

Dynamic Role of Cluster Cocatalysts on Molecular Photoanodes for Water Oxidation

Jingguo Li,¹ Wenchao Wan,¹ C. A. Triana,¹ Zbynek Novotny,² Jürg Osterwalder,² Rolf Erni,³
Greta R. Patzke*¹

¹Department of Chemistry, University of Zurich, Winterthurerstrasse 190, CH-8057 Zurich, Switzerland.

² University of Zurich, Department of Physics, Winterthurerstrasse 190, CH-8057 Zurich, Switzerland.

³Electron Microscopy Center, Empa, Swiss Federal Laboratories for Materials Science and Technology, CH-8600 Dübendorf, Switzerland

E-mail: greta.patzke@chem.uzh.ch

Table of Contents

1.	Underlying multiple dynamic competing processes on hematite photoanodes.....	3
2.	Materials	3
3.	Analytical Characterizations	4
4.	Synthesis, characterization and initial screening of hematite photoanodes	4
5.	Synthesis of molecular cubanes	7
6.	Fabrication of hematite photoanodes loaded with cocatalysts	10
7.	(Photo)electrochemical characterization of bare and C₁ loaded photoanodes.....	10
a.	Photoelectrochemical activity determination	10
b.	Transient photocurrent spectra (TPS) measurement and analysis	11
c.	Intensity-modulated TPS (IM-TPS) measurements and analysis	13
d.	Kinetic analysis of both anodic and cathodic decay processes.....	18
e.	Photoelectrochemical impedance spectra (PEIS) and intensity-modulated EIS measurement	23
8.	(Photo)electrochemical characterization of C₂ loaded photoanodes.....	25
a.	TPS, IM-TPS and respective kinetic analysis	27
b.	PEIS, IM-EIS and respective kinetic analysis	32
9.	(Photo)electrochemical characterization of C₃ loaded photoanodes.....	33

a.	TPS, IM-TPS and respective kinetic analysis	33
b.	PEIS, IM-EIS and respective kinetic analysis	37
10.	(Photo)electrochemical measurement of C₄ loaded photoanodes.....	38
a.	TPS, IM-TPS and respective kinetic analysis	39
b.	PEIS, IM-EIS and respective kinetic analysis	43
11.	Stability characterization of molecular cocatalysts modified photoanode	44
a.	(Photo)electrochemical study	44
b.	HAADF-STEM studies	47
c.	X-ray photoelectron spectroscopy (XPS) studies	48
References.....		51

1. Underlying multiple dynamic competing processes on hematite photoanodes

Ideally, after photo-excited charge separation (k_{sep}), all photo-generated electrons (e^-) are first transported to substrate electron collector and then accumulated on the photocathode surface for the water reduction reaction. Meanwhile, all photo-generated holes (h^+) migrate to photoanode surface (k_{transp}) and participate in the water oxidation reaction (k_{transf}) directly through hematite surface states or surface loaded cocatalysts. However, processes like electron hole recombination at the semiconductor/substrate interface ($k_{rec, semi/sub}$), in bulk hematite ($k_{rec, bulk}$) and on the hematite surface ($k_{rec, surface}$) can significantly deteriorate the forward hole transfer efficiency. All these kinetic parameters associated with the above-mentioned processes are actually forming a ‘dynamic equilibrium’ network at steady-state conditions, which implies that it is not possible to arbitrarily modulate one parameter without affecting the others. Taking into account this dynamic nature is the key to understand the actual role of surface loaded cocatalysts.

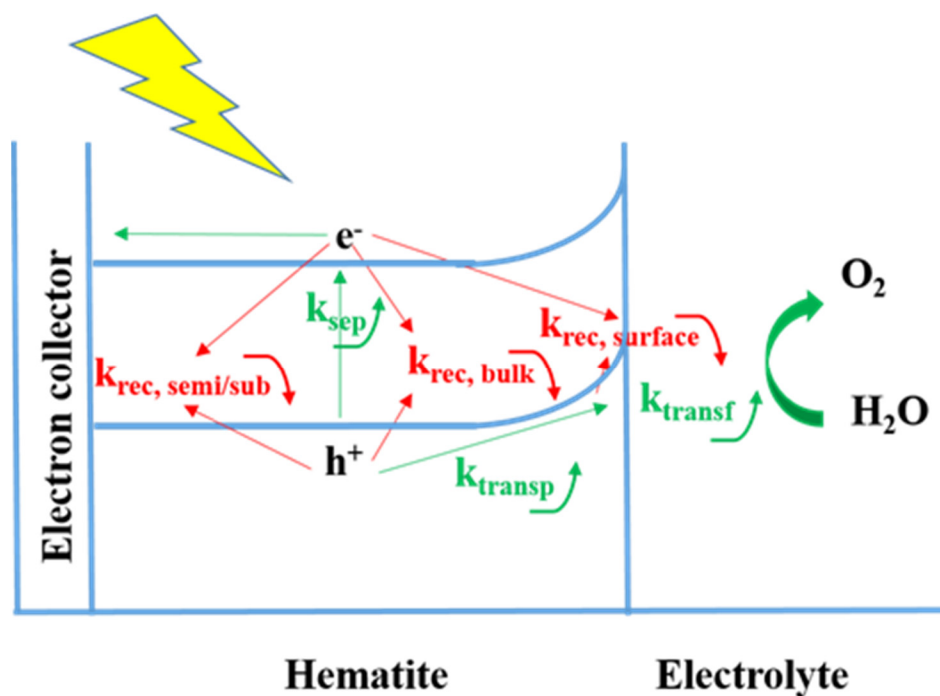


Figure S1. Schematic working principle and charge carrier pathways on hematite photoanodes for water oxidation.

2. Materials

Ferric chloride ($FeCl_3 \cdot 6H_2O$, > 99%), cobalt chloride ($CoCl_2 \cdot 6H_2O$, > 99%), sodium nitride, Nafion® 117 solution (~5% in a mixture of low aliphatic alcohols and water) and fluorine-doped tin oxide coated glasses (FTO, surface resistivity $\sim 8 \Omega/sq$) were obtained from Sigma-Aldrich. Ethanol (99.7%) and acetone

(99.5%) were obtained from Reuss Chemie. Reagents were all used as received. Deionized water was used throughout the experiments.

3. Analytical Characterizations

Powder X-ray diffraction (PXRD) patterns for molecular cubane samples were recorded on a STOE STADI P powder diffractometer (Ge monochromator), operated in transmission mode, with Cu-K α radiation at ($\lambda = 1.54056 \text{ \AA}$), while for hematite samples grown on FTO surfaces, a Rigaku smartlab diffractometer (reflection mode) was used. Raman spectra were recorded on a Renishaw System 2000 (532 nm laser with spot size $\sim 2 \text{ }\mu\text{m}$). Scanning electron microscopy (SEM) images were obtained using a SEM-Zeiss Supra 50 VP which was coupled with an energy dispersive X-ray spectroscopy (EDX) detector (genesis). UV-Vis spectra were recorded on a Lambda 650 S Perkin Elmer UV-visible spectrometer in the range 300-800 nm using a Quartz SUPRASIL precision cell (10 mm). Attenuated total reflection Fourier-transform (ATR-FT-IR) spectra were recorded on a Bruker Vertex 70 spectrometer equipped with a Platinum ATR accessory containing a diamond crystal. The pH value was measured with a Model pHs-3C meter (Mettler Toledo FE20). All (photo)electrochemical tests were carried out on a Zahner Zennium electrochemical workstation and data was analyzed using the Thales software provided by Zahner. An AM 1.5 solar simulator (LOT Quantum Design AG) was used for all photoelectrochemical tests. The illumination light intensity on the surface of the photoanodes was controlled by the distance between light source and photoanode surface, and the illumination intensity was quantified using a solar detector (LOT Quantum Design AG). A mechanical beam shutter coupled with a K-cube Solenoid controller (Thorlabs GmbH) was used for modulating the solar irradiation, and it took 10 ms for the shutter to open 20% to 80% exposure. A three electrode cell was used with Ag/AgCl (in saturated KCl solution) and Pt wire as reference and counter electrodes, while 0.05 M borate buffer was employed as electrolyte for all measurements. For EIS tests, a frequency range from 0.1 to 10,000 Hz was selected with an AC voltage amplitude of 5 mV.

4. Synthesis, characterization and initial screening of hematite photoanodes

Commercial fluorine doped tin oxide coated glass slides (FTO, 3 mm thickness with surface resistivity $\sim 8 \text{ }\Omega/\text{sq}$) were first cut into small pieces ($1.5 \cdot 2 \text{ cm}$). Then they were washed with the following solvents (30 min each with sonication) subsequently: deionized water, ethanol, acetone and deionized water. The growth of nanostructured FeOOH on the FTO surface was performed according to a previously reported method.^{1,2} Generally, 5 mL of a freshly prepared FeCl₃ (0.15 M) and NaNO₃ (1 M) mixture in deionized water was added to a Teflon inlet and one piece of clean FTO glass was put into the reactor with the conductive side facing down. Then these Teflon inlets were loaded into a stainless steel hydrothermal reactor and closed tightly. The reactors were heated up to 100 °C for 6 h and cooled down naturally to room temperature. The surface coated FeOOH FTO samples were washed with large amounts of deionized water

before drying in air. Hematite photoanodes were obtained by calcination of these FeOOH FTO samples at 800 °C for 10 min.^{3,4}

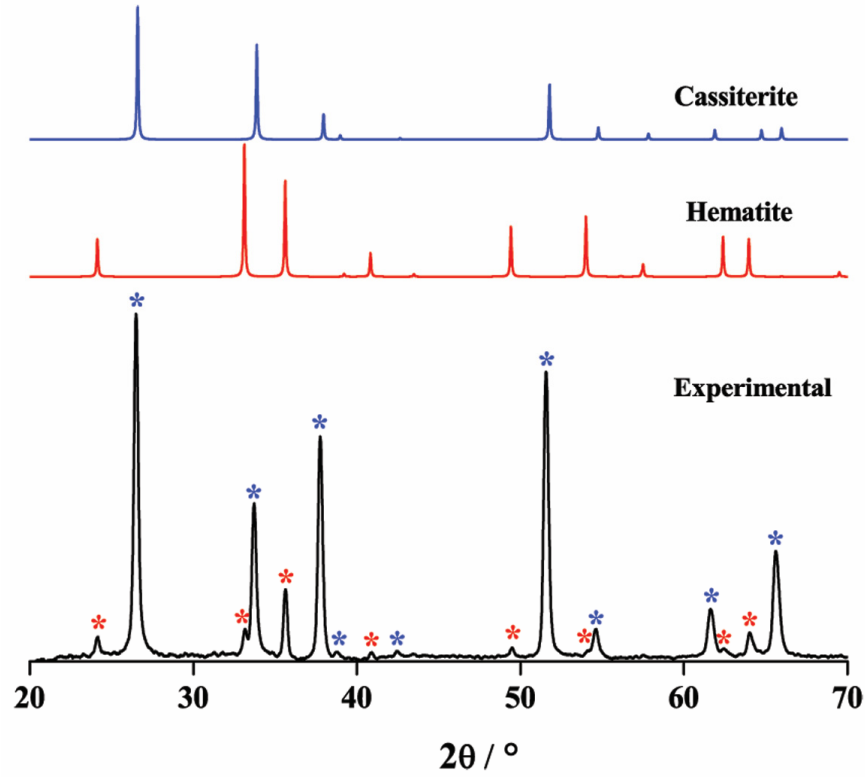


Figure S2. Experimental thin film XRD pattern of hematite photoanode (bottom, blue and red stars are diffraction peaks from hematite and cassiterite, respectively.), standard hematite (middle, from Crystallography Open Database, code: 900139), and standard cassiterite (from American Mineralogist Crystal Structure Database, code: 0011761).

The band gap of hematite was determined from the absorbance data recorded in the range of 350-800 using the Tauc equation:

$$\alpha h\nu = A_0(h\nu - E_g)^n$$

where A_0 is a constant, $h\nu$ is the photon energy (eV), and E_g is the band gap (eV). The value of n is related to the nature of the optical transition: n equals 0.5 or 1.5 for direct allowed/forbidden transitions, and n equals 2 or 3 for indirect allowed/forbidden transitions, respectively.

α is the optical absorption coefficient, which could be derived from absorbance (A) and hematite film thickness (t) using the expression:

$$\alpha = 2.303A/t$$

The band gap of as-prepared hematite photoanodes could be estimated from the linear fit of $(\alpha h\nu)^n$ vs. incident photon energy ($h\nu$) near the absorption edge. The determined indirect band energies were in line with the reported values.

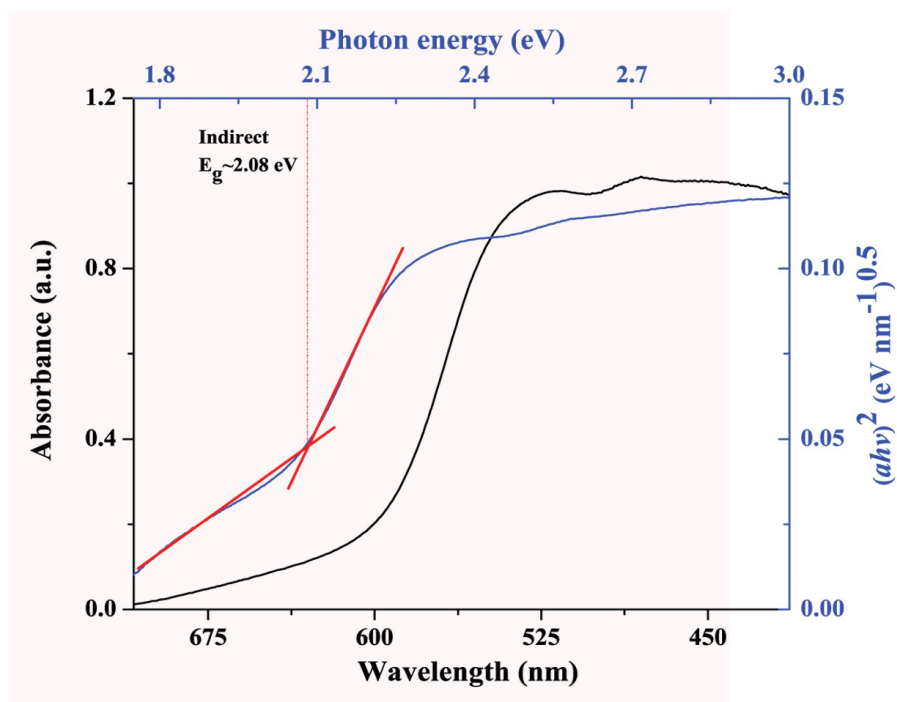


Figure S3. UV-Vis absorbance spectra and derived indirect allowed transition band gap energy of fabricated hematite photoanode.

5. Synthesis of molecular cubanes

The molecular cubanes $[\text{Co}^{\text{II}}_4(\text{dpy}\{\text{OH}\}\text{O})_4(\text{OAc})_2(\text{H}_2\text{O})_2](\text{ClO}_4)_2$ (C_1) $[\text{Co}^{\text{II}}_4(\text{hmp})_4(\mu\text{-OAc})_2(\mu_2\text{-OAc})_2(\text{H}_2\text{O})_2]$ (C_2) (hmp = 2-(hydroxymethyl)pyridine), and $[\text{Co}^{\text{II}}_3\text{Er}(\text{hmp})_4(\text{OAc})_5\text{H}_2\text{O}]$ (C_3) were synthesized and crystallized according to our previous publications.⁵⁻⁷

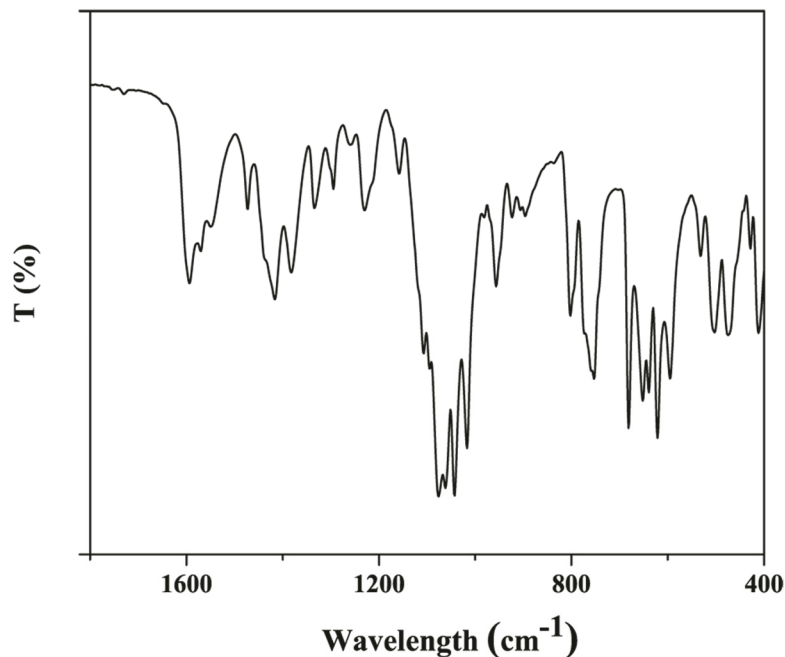


Figure S4. ATR-FT-IR spectrum of molecular cubane C_1 .

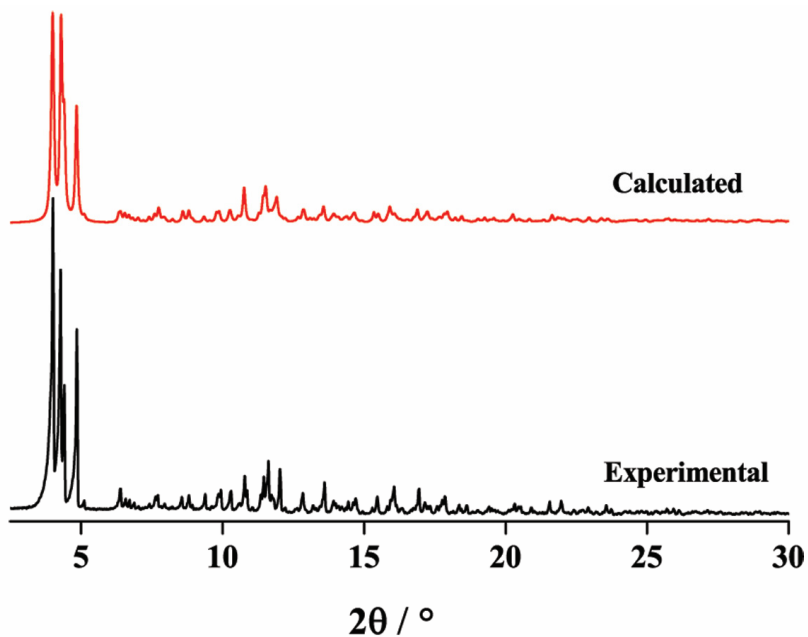


Figure S5. Experimental and calculated PXRD pattern of C_1 .

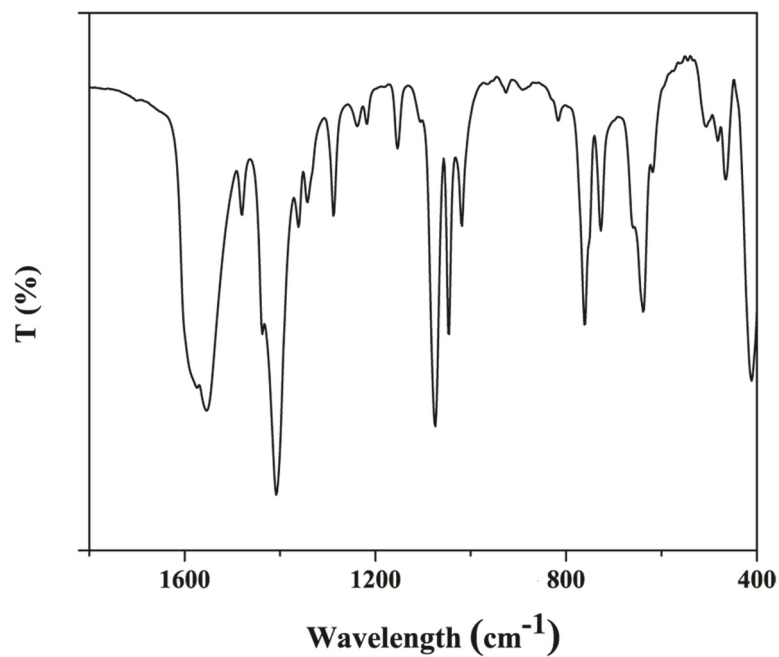


Figure S6. ATR-FT-IR spectrum of molecular cubane C_2 .

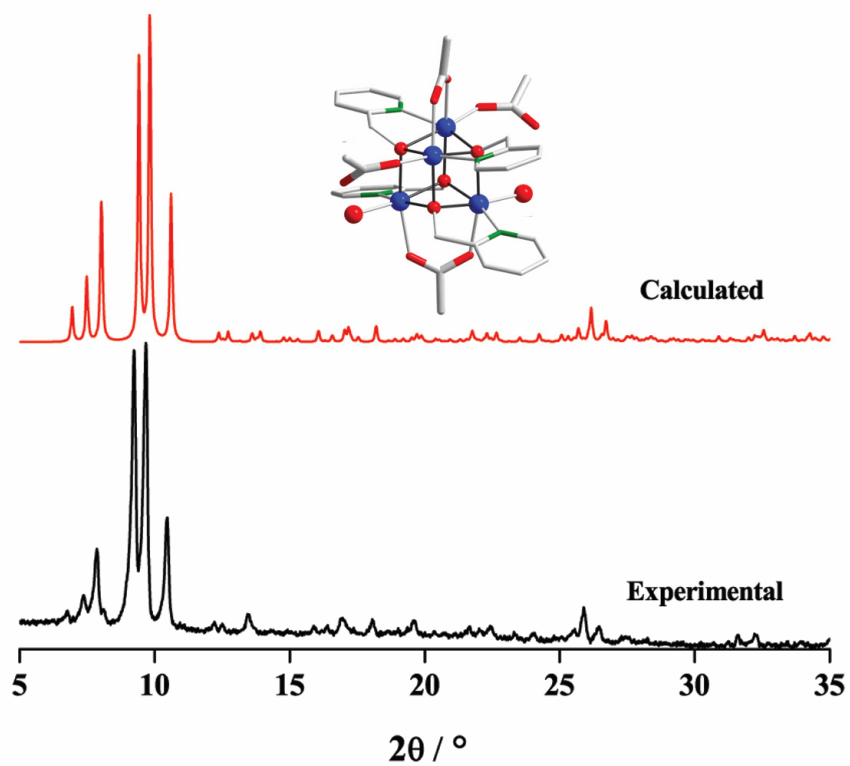


Figure S7. Experimental and calculated PXRD pattern of C_2 (inset: crystal structure of C_2 ; Co: dark blue, C: gray, O: red, N: green).

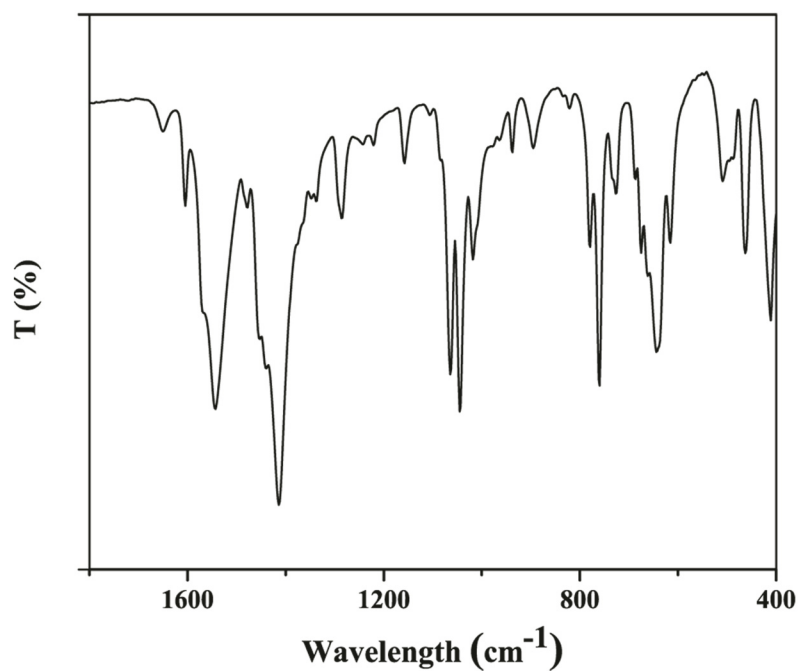


Figure S8. ATR-FT-IR spectrum of molecular cubane C_3 .

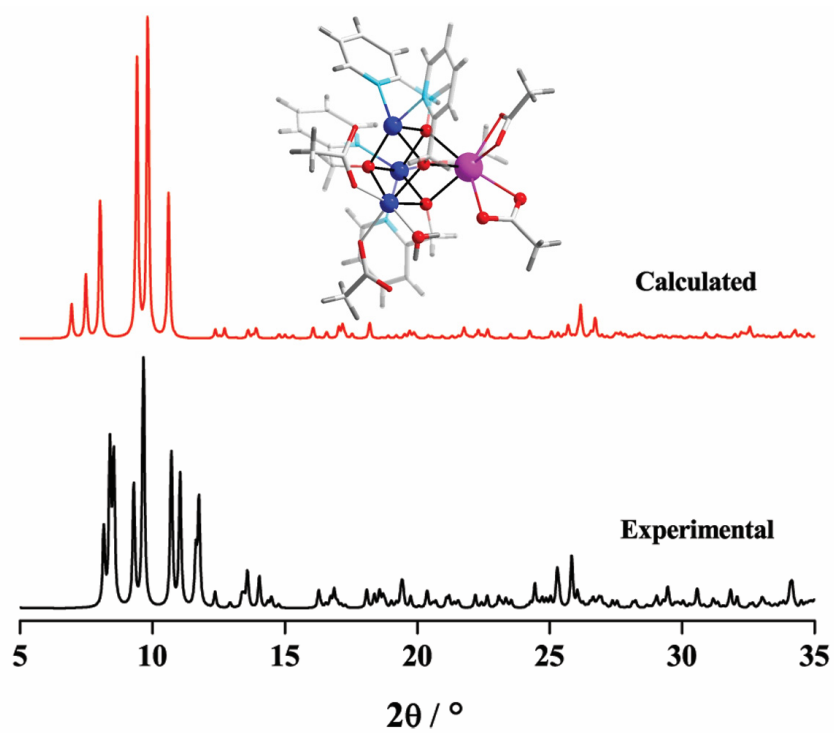


Figure S9. Experimental and calculated PXRD pattern of C_3 (inset: crystal structure of C_3 ; Co: dark blue, Er: purple, C: white, O: red, N: green, H: gray).

6. Fabrication of hematite photoanodes loaded with cocatalysts

Nafion was used as physical binder for the loading of molecular cubane catalysts. In a representative procedure (taking C₁ as an example), Nafion solution (5%) was diluted to 0.5% with 0.05 M borate buffer (pH 8.5) and then different amounts of C₁ were added and sonicated until a clear solution was obtained. 10 μ L of these mixtures were casted onto the pre-screened hematite surfaces. The density of C₁ was determined to be 3.3 to 53.3 nmol cm⁻².

Nomenclature: Bare hematite photoanodes are abbreviated as H, Nafion modified hematite photoanodes are labeled as H-N, and different amounts of C₁ loaded hematite are indicated from H-N-C₁-3.3 nmol cm⁻² to H-N-C₁-53.3 nmol cm⁻², respectively.

7. (Photo)electrochemical characterization of bare and C₁ loaded photoanodes

a. Photoelectrochemical activity determination

LSV for all photoanodes were recorded in 0.05 mM pH 8.5 borate buffer, using Pt wire and Ag/AgCl (saturated) as counter and reference electrode. Front illumination was adopted for all photoelectrochemical measurements. The contribution of the photocurrent from the leached Pt species (from Pt counter electrode) could be excluded due to its high water oxidation overpotentials.

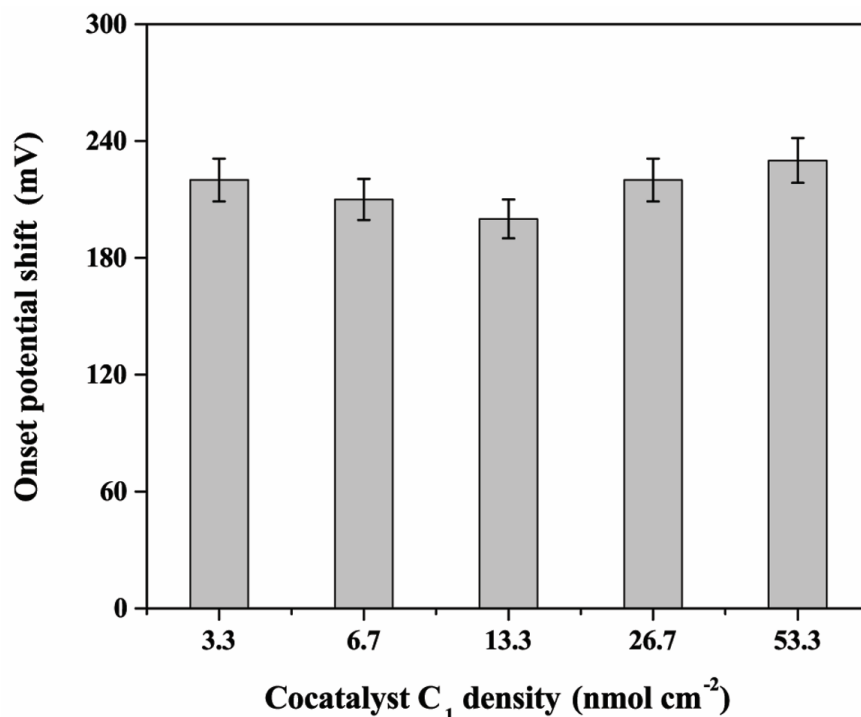


Figure S10. Cathodic onset potential shift of different amount of C₁ loaded photoanodes.

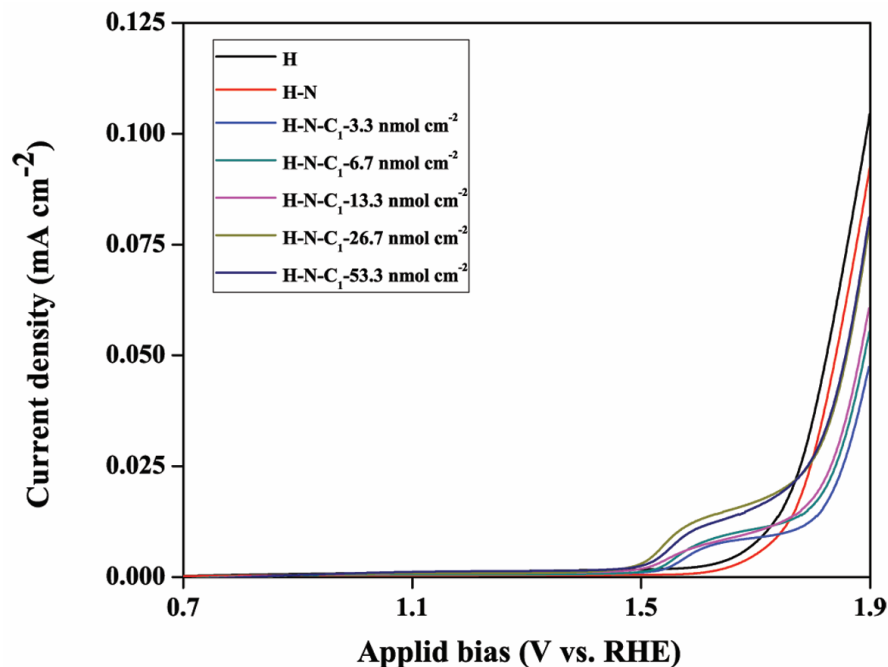


Figure S11. J - V curves of photoanodes with different C_1 loading density under dark conditions in 0.05 M borate buffer (pH 8.5). Scan rate: 10 mV s⁻¹.

b. Transient photocurrent spectra (TPS) measurement and analysis

TPS measurements for all photoanodes were started from steady state in dark conditions. After light on, a sufficient time interval was provided for achieving steady state at photoelectrochemical conditions. The same strategy was applied for the light off process. An automatic beam shutter with K-cube controller was used to initiate both light on and off processes. The TPS measurement for every photoanode was performed several times at constant applied bias to minimize the systematic error.

The amount of charges passed through the photoelectrode during both anodic (Q_{anodic}) and cathodic ($Q_{cathodic}$) transient processes were obtained by integration of the current density curve for the respective decay time intervals. This was achieved with the built-in function of the Thales software. J_{anodic} and $J_{cathodic}$ represent the peak current during anodic and cathodic transient processes, respectively. J_{ss} stands for the steady-state photocurrent under illumination conditions.

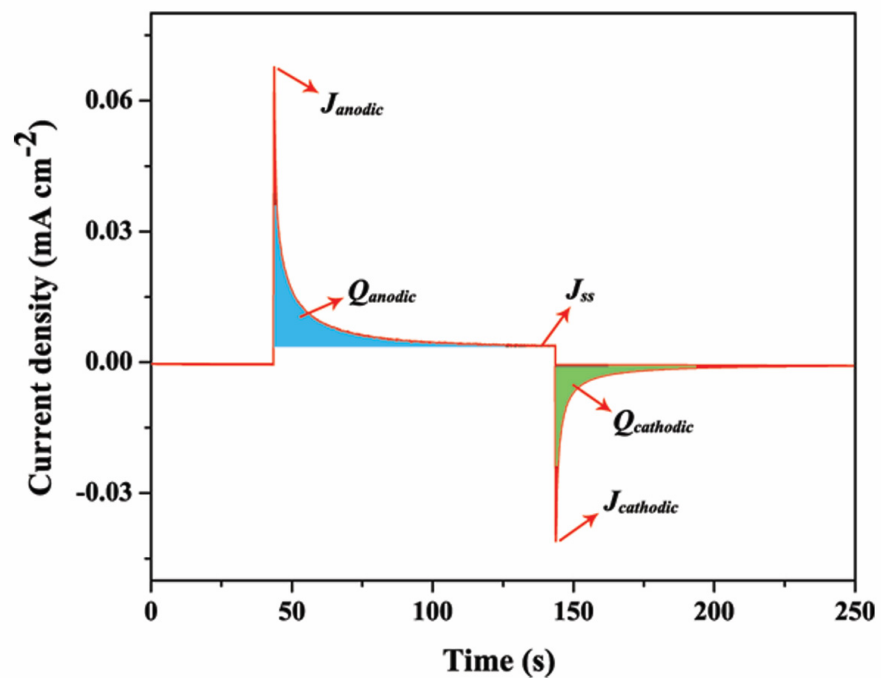


Figure S12. Schematic illustration of how TPS recording and analysis; Q_{anodic} and $Q_{cathodic}$ were determined from integration of current density curves with the time interval of transient process, using the built-in function of the Thales software.

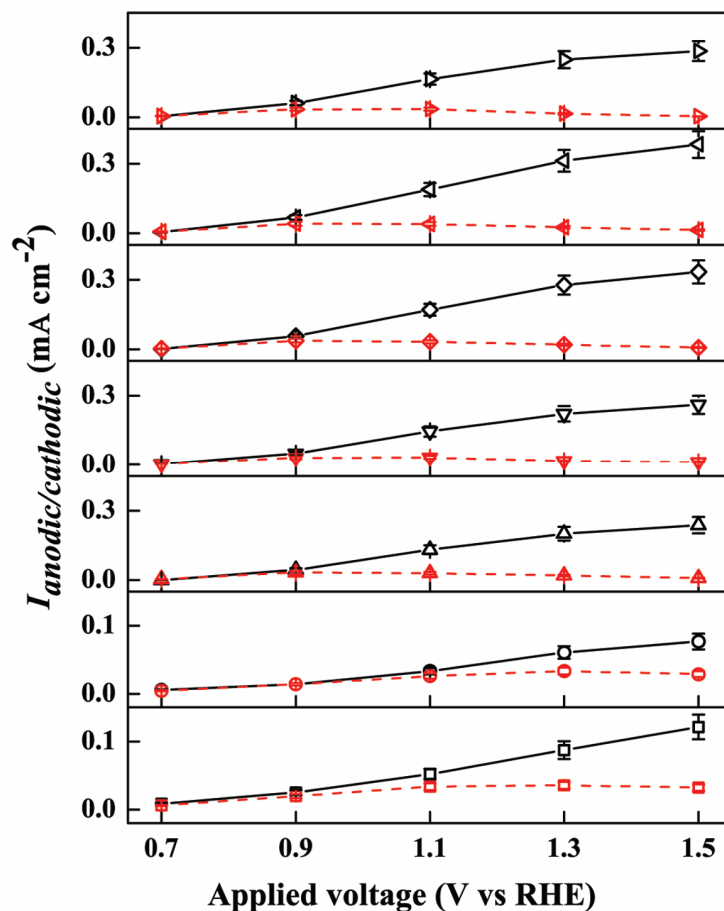


Figure S13. Transient J_{anodic} and $J_{cathodic}$ for bare and C_1 loaded photoanodes (bottom to top: bare photoanode, followed by C_1 modified photoanodes with increasing loading density from 0 to $53.3 \text{ nmol cm}^{-2}$; black solid line and red dashed lines = anodic and cathodic processes, respectively.) Transient experiments were conducted at various constant biases vs. RHE in 0.05 M borate buffer (pH 8.5), and an AM 1.5 G solar simulator at 100 mW cm^{-2} was used for illumination.

c. Intensity-modulated TPS (IM-TPS) measurements and analysis

IM-TPS measurements were carried out under the same conditions as described in the TPS section, except that series of different light intensity ($6\text{-}100 \text{ mW/cm}^2$) were applied. The intensity change was achieved by tuning the distance of sample surface to the solar simulator source via a track. Light intensities were quantified using a solar detector.

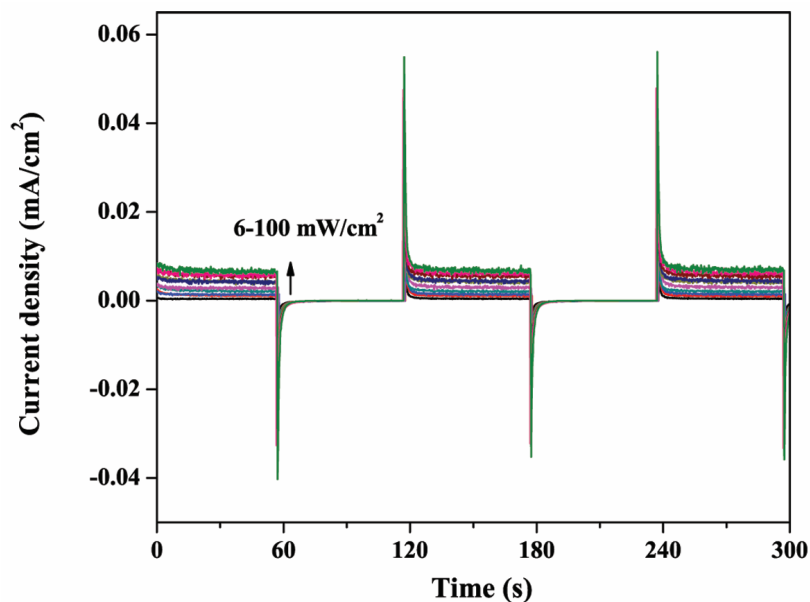


Figure S14. Transient spectra for bare hematite photoanodes measured under modulated illumination intensities in 0.05 M borate buffer (pH 8.5) at a constant applied bias of 0.9 V vs. RHE. The illumination intensity was controlled by tuning the distance between light source and photoanode surface.

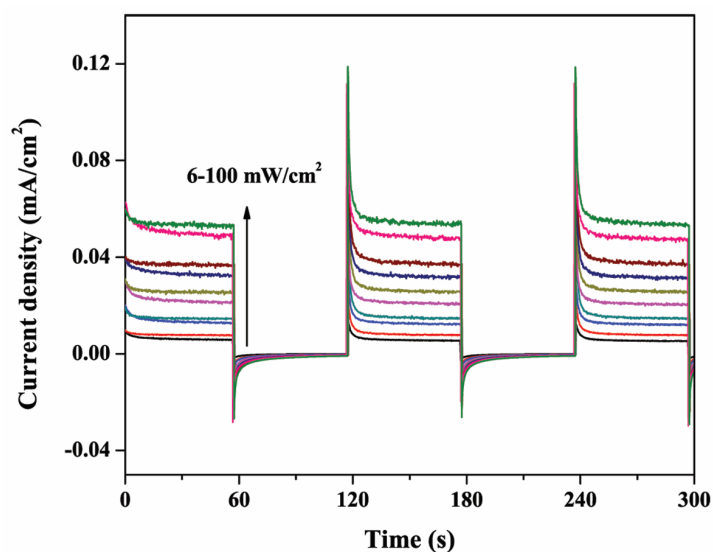


Figure S15. Transient spectra for C₁ loaded photoanodes (26.7 nmol cm⁻²) measured under modulated illumination intensities in 0.05 M borate buffer (pH 8.5) at a constant applied bias of 0.9 V vs. RHE. The illumination intensity was controlled by tuning the distance between light source and photoanode surface.

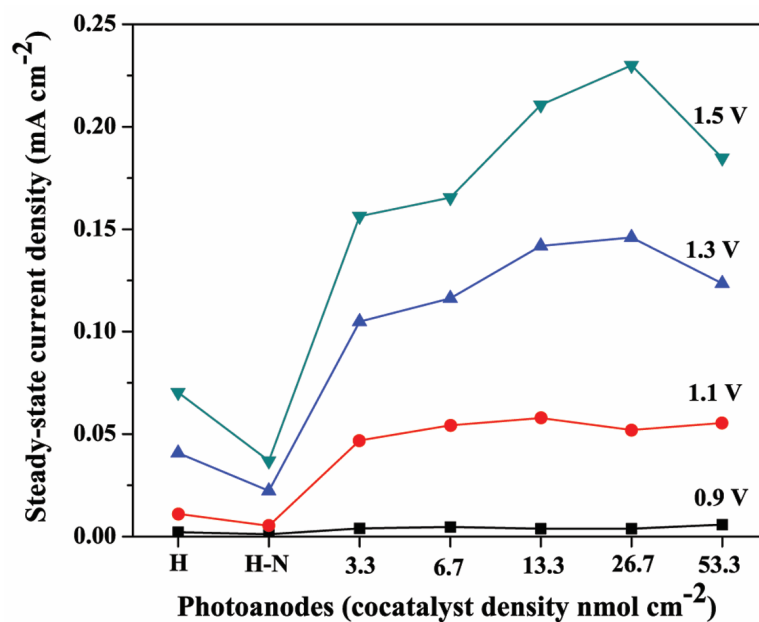


Figure S16. Comparison of steady state photocurrent density for C₁ loaded and bare hematite photoanodes at various applied biases. The steady state photocurrent density value was adopted from the anodic transient measurement where the photocurrent density did not show any noticeable decrease after light on. Clearly, the surface coated Nafion thin film had a negative effect on the steady state photocurrent density which is possibly due to the partial blockage of catalytically active centers on the hematite photoanode surface.

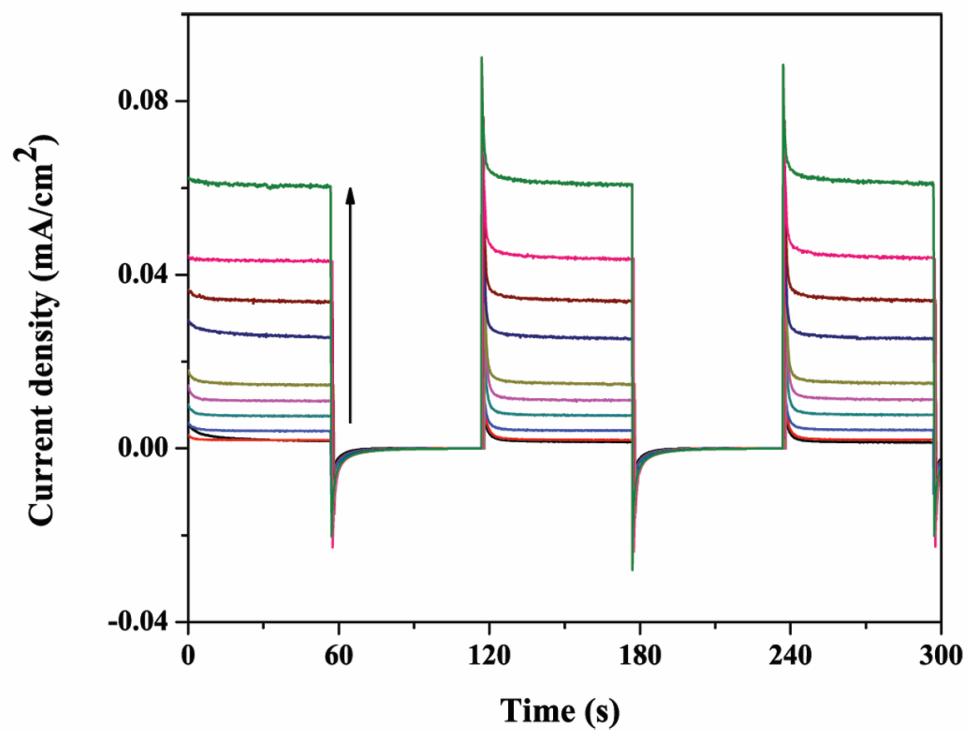


Figure S17. Transient spectra for bare hematite photoanode measured under modulated illumination intensities in 0.05 M borate buffer (pH 8.5) at a constant applied bias of 1.3 V vs. RHE. The illumination intensity was controlled by tuning the distance between light source and photoanode surface.

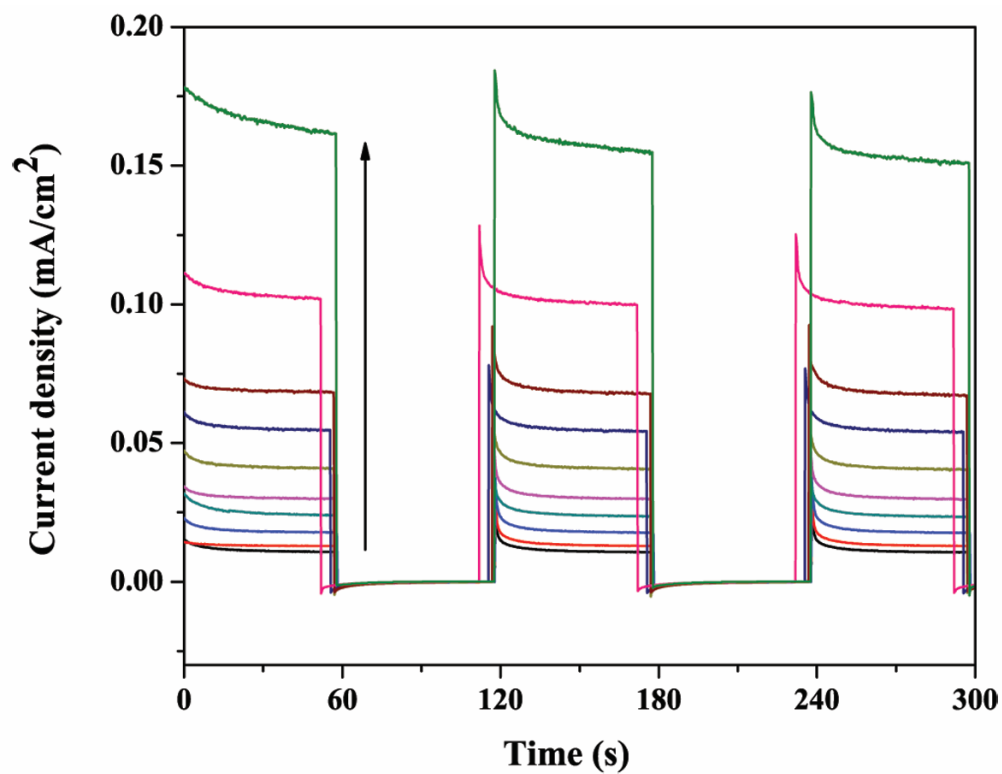


Figure S18. Transient spectra for C₁ loaded photoanode (26.7 nmol cm⁻²) measured under modulated illumination intensities in 0.05 M borate buffer (pH 8.5) at a constant applied bias of 1.3 V vs. RHE. The illumination intensity was controlled by tuning the distance between light source and photoanode surface.

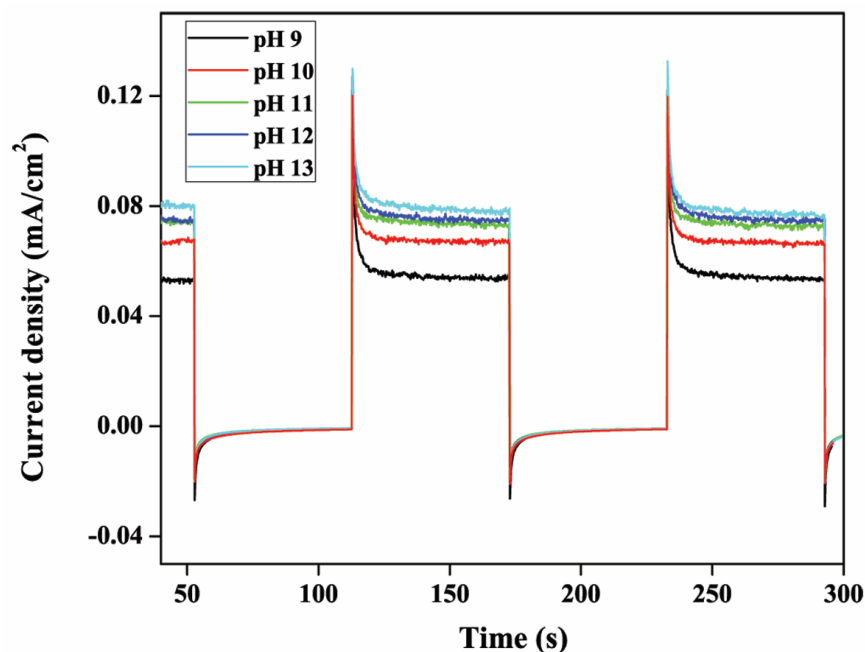


Figure S19. Transient spectra for C₁ loaded photoanode (26.7 nmol cm⁻²) measured at various pH values (50 mM borate buffer) at a constant applied bias of 0.9 V vs. RHE. An AM 1.5G solar simulator at 100 mW cm⁻² was used for illumination.

d. Kinetic analysis of both anodic and cathodic decay processes

At steady state photoelectrochemical conditions, the surface accumulated hole density is in a dynamic steady state as well, resulting from the equilibrium of processes like photo-induced charge separation, electron hole recombination and hole transfer for water oxidation. All these processes should proceed with constant rate at steady state photoelectrochemical conditions, and the rates of these different processes are all closely related to the steady state surface hole density. Thus, the relationship of steady state photocurrent density with surface hole density can be described with equation S1:

$$J_{ss} = k_{app} * [h^+]^n \quad \text{Equation S1}$$

J_{ss} stands for steady-state photocurrent density, k_{app} is the apparent reaction rate constant associated to water oxidation reaction, $[h^+]$ is the surface accumulated hole density at steady-state conditions, and n is the reaction order with respect to surface holes.

To understand the underlying dynamic interplay of forward hole accumulation/transfer and back electron hole recombination processes, both anodic and cathodic transient decay curves were fitted with the following bi-phase exponential decay function, consisting of a fast exponential decay phase coupled with a slow exponential one.^{8,9} It is important to point out that both fast and slow decay phases are closely related

to the previously mentioned competing processes. The characteristic evolution feature for forward hole accumulation (descending) and transfer dynamics (rising) during the anodic transient process determines the separation between fast and slow decay phase. The decay lifetimes τ_1 and τ_2 for both fast and slow decay stages could be derived with the following equation:

$$J_i = A_1 e^{\frac{-(t-t_0)}{\tau_1}} + A_2 e^{\frac{-(t-t_0)}{\tau_2}} + J_0 \quad \text{Equation S2}$$

In this equation, J_i is the probed current density during the transient decay process; A_1 and A_2 are the respective absolute value of maximum achievable photocurrent for fast and slow decay processes. The decay lifetimes τ_1 and τ_2 are actually representing the competing hole accumulation/transfer and recombination kinetics in both fast and slow decay phase:

$$\tau_1 = \frac{1}{k_{ct1} + k_{rec1}} \quad \text{Equation S3}$$

$$\tau_2 = \frac{1}{k_{ct2} + k_{rec2}} \quad \text{Equation S4}$$

To interpret the kinetic parameters during both fast and slow decay phase, the previously adopted functions^{10,11} were used as follows:

$$\frac{J_\infty}{J_{i1}} = \frac{k_{ct1}}{k_{ct1} + k_{rec1}} \quad \text{Equation S5}$$

$$J_{i1} = A_1 e^{\frac{-(t-t_0)}{\tau_1}} + J_0 \quad \text{Equation S6}$$

$$\frac{J_\infty}{J_{i2}} = \frac{k_{ct2}}{k_{ct2} + k_{rec2}} \quad \text{Equation S7}$$

$$J_{i2} = A_2 e^{\frac{-(t-t_0)}{\tau_2}} + J_0 \quad \text{Equation S8}$$

J_∞ is the probed current density after the decay process, and the J_{i1} and J_{i2} values were calculated using Equations S6 and S8.

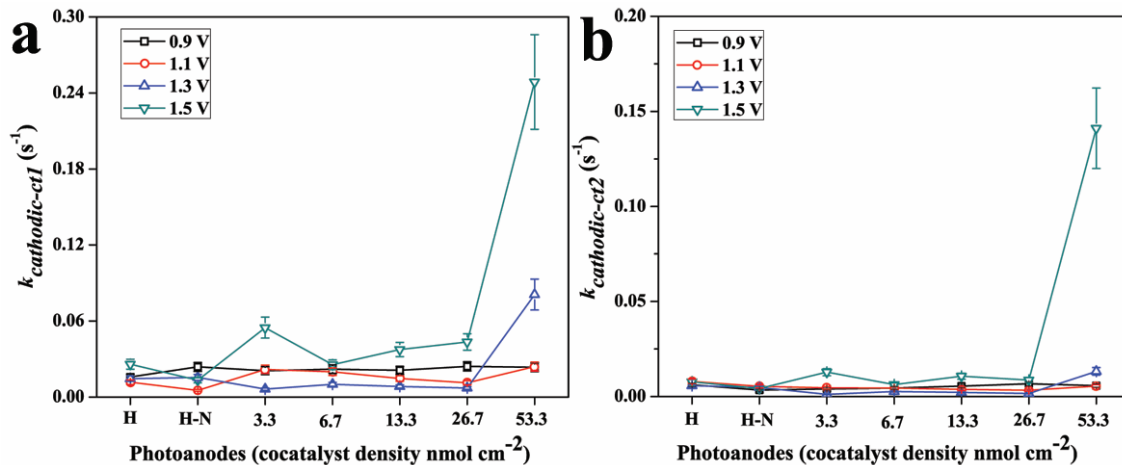


Figure S20. Comparison of the cathodic forward hole accumulation/transfer rate constants for C₁ loaded and bare hematite photoanodes during the fast decay phase $k_{cathodic-ct1}$ (a) and slow decay phase $k_{cathodic-ct2}$ (b). The anodic transient process was initiated by turning light off at constant applied biases vs. RHE, in 0.05 M borate buffer solution.

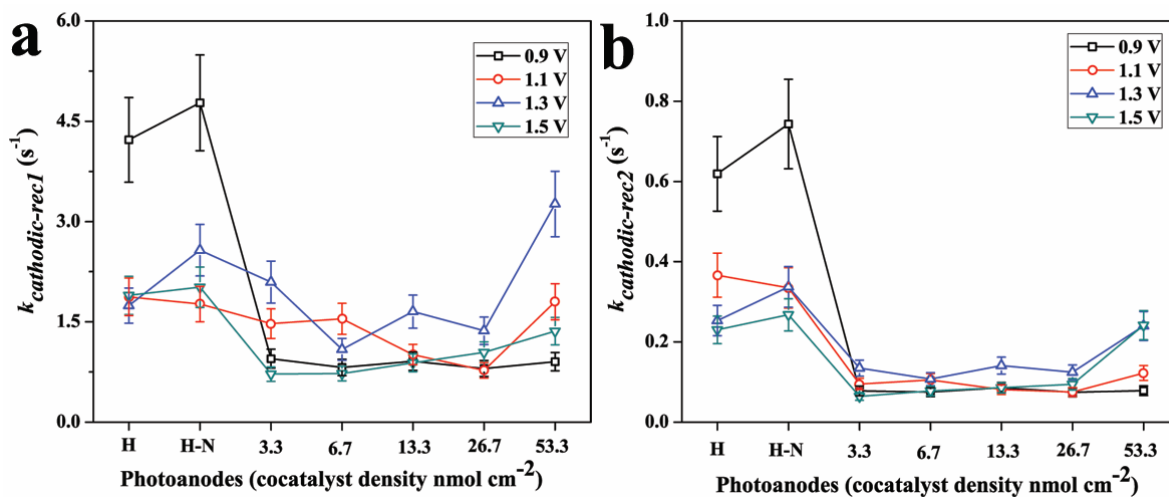


Figure S21. Comparison of the cathodic back-electron hole recombination rate constants for C₁ loaded and bare hematite photoanodes during the fast decay phase $k_{cathodic-rec1}$ (a) and slow decay phase $k_{cathodic-rec2}$ (b). The anodic transient process was initiated by turning the light off at constant applied biases vs. RHE, in 0.05 M borate buffer solution.

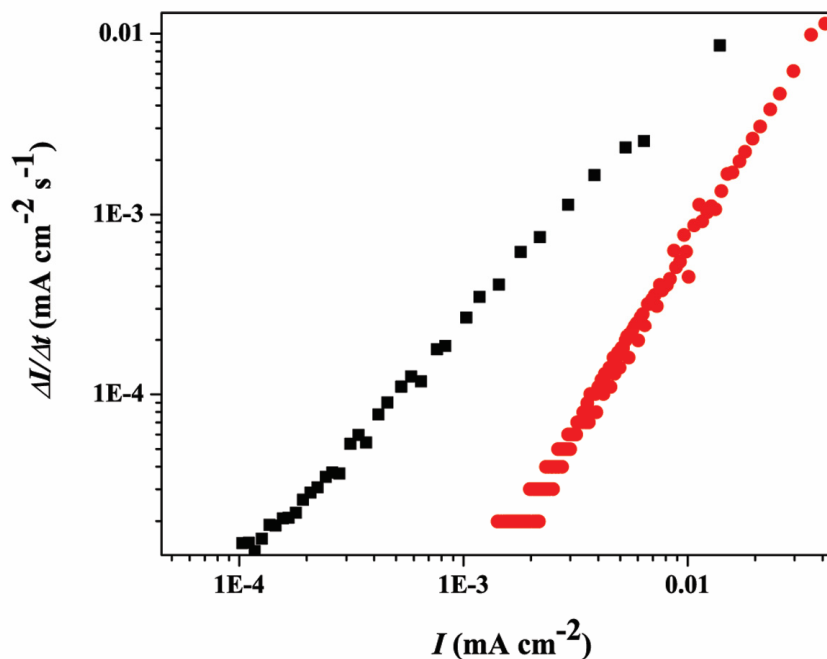


Figure S22. Determination of the cathodic transient current density decay kinetics at 0.9 V vs. RHE (in terms of slopes) for bare (black squares) and C₁ loaded (26.7 nmol cm⁻²) photoanodes (red circles). The magnitude of current density probed during the cathodic decay was plotted against the current density change at different time intervals. This faster decay kinetics for photoanodes loaded with cocatalysts clearly indicate that the decay kinetics are actually closely related to the surface accumulated hole density. The surface loaded C₁ molecules are able to store photo-generated holes, which can however still undergo recombination process.

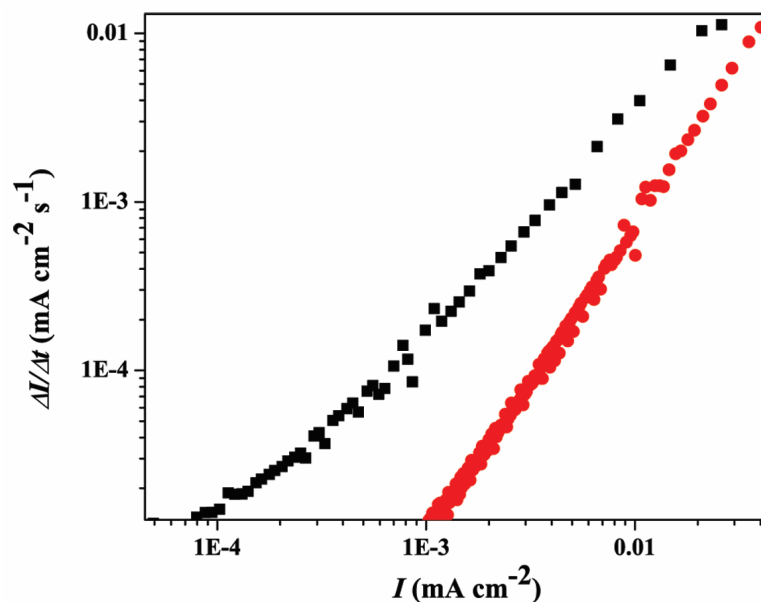


Figure S23. Determination of the cathodic transient current density decay kinetics at 1.1 V vs. RHE (in terms of slopes) for bare (black squares) and C_1 loaded ($26.7 \text{ nmol cm}^{-2}$) photoanodes (red circles). The magnitude of current density probed during the cathodic decay was plotted against the current density change at different time intervals.

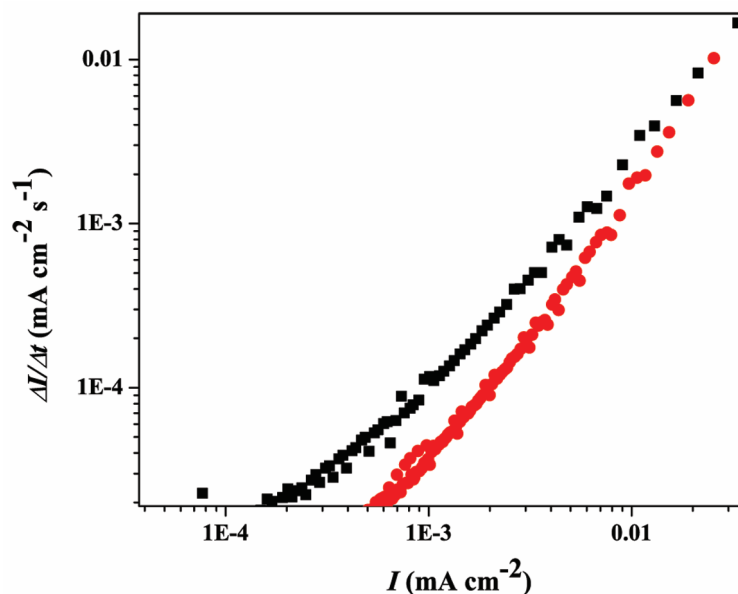


Figure S24. Determination of the cathodic transient current density decay kinetics at 1.3 V vs. RHE (in terms of slopes) for bare (black squares) and C_1 loaded ($26.7 \text{ nmol cm}^{-2}$) photoanodes (red circles). The magnitude of current density probed during the cathodic decay was plotted against the current density change at different time intervals.

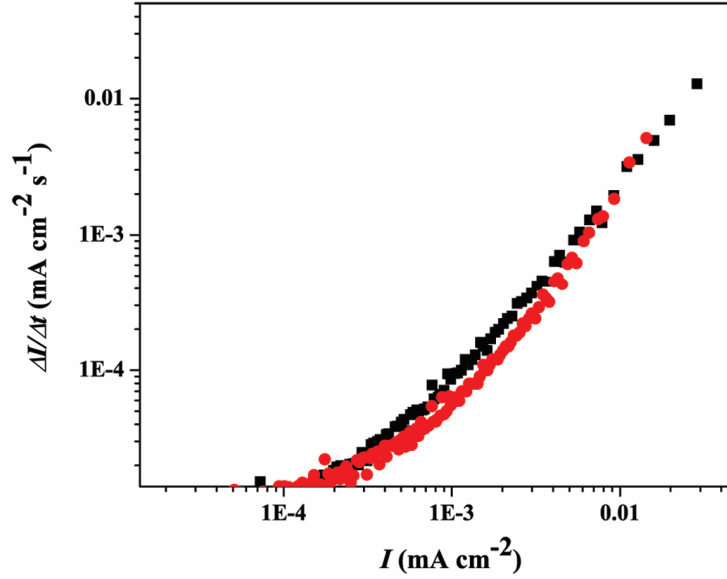


Figure S25. Determination of the cathodic transient current density decay kinetics at 1.5 V vs. RHE (in terms of slopes) for bare (black squares) and C₁ loaded (26.7 nmol cm⁻²) photoanodes (red circles). The magnitude of current density probed during the cathodic decay was plotted against the current density change at different time intervals.

e. Photoelectrochemical impedance spectra (PEIS) and intensity-modulated EIS measurement

PEIS data were gathered using a 5 mV amplitude perturbation with frequencies between 0.01 and 10000 Hz. Data was fit with the built-in function of Thales software.

Intensity-modulated EIS (IM-EIS) was performed under the same conditions as PEIS measurements, except for using different illumination intensities:

$$[h^+] = \left[C_{ct} * V_{applied} * \left(\frac{R_{ct}}{R_{ct} + R_{bulk} + R_s} \right) \right] / S \quad \text{Equation S9}$$

where $[h^+]$ is the surface hole density, C_{ct} is the charge transfer capacitance, $V_{applied}$ is the applied voltage during IM-EIS measurement, S is the active surface area measured. R_{ct} , R_{bulk} and R_s are resistances related to surface charge transfer, bulk hematite and electrolyte, respectively.

For kinetic analysis, when both charge transfer recombination kinetics (k_{ct} and k_{rec}) are assumed to be inversely proportional to their respective measured resistances (R_{ct} and R_{bulk}),^{12,13} then the portion of charge transfer during the near-steady state PEIS measurement could be estimated from the following equation:

$$\frac{k_{ct}}{k_{ct} + k_{rec}} = \frac{1}{1 + R_{ct}/R_{bulk}} \quad \text{Equation S10}$$

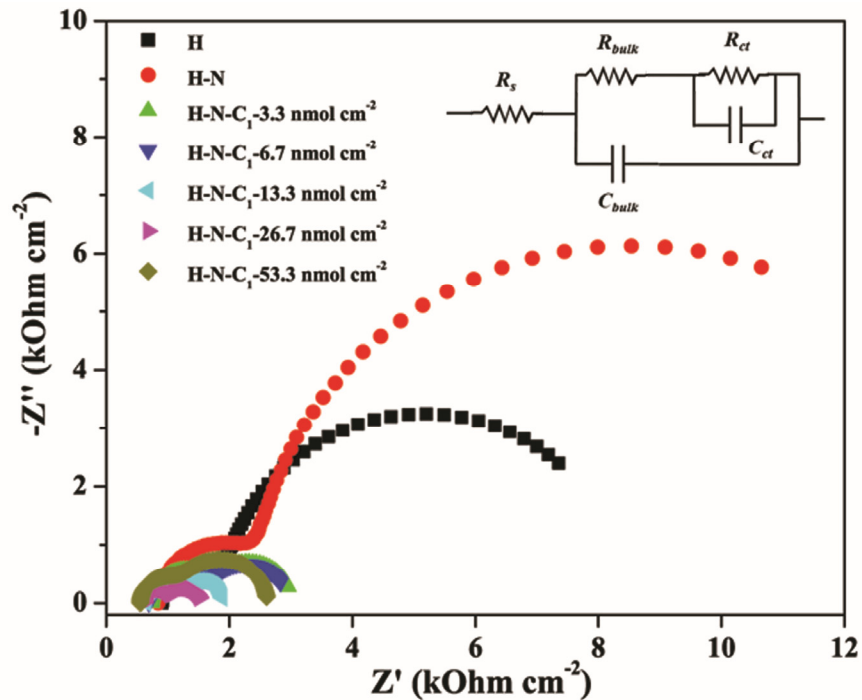


Figure S26. Nyquist plots for C_1 loaded and bare hematite photoanodes measured under AM 1.5 G simulated sunlight at 100 mW cm^{-2} in 0.05 M borate buffer (pH 8.5), inset: equivalent electric circuit (EC) used for interpretation of the measured data (C_{bulk} standing for capacitance of bulk hematite, C_{ct} representing the capacitance for surface charge transfer, R_{bulk} and R_{ct} are related resistors).

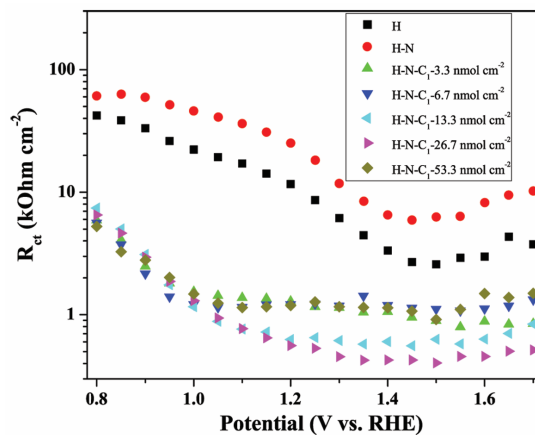


Figure S27. R_{ct} (b) values of C_1 loaded and bare hematite photoanodes fitted from impedance spectra measured under AM 1.5 G simulated sunlight at 100 mW cm^{-2} in 0.05 M borate buffer (pH 8.5) at different applied potentials. Experimental details: frequency, 0.1 to 10000 Hz with 5 mV amplitude perturbation.

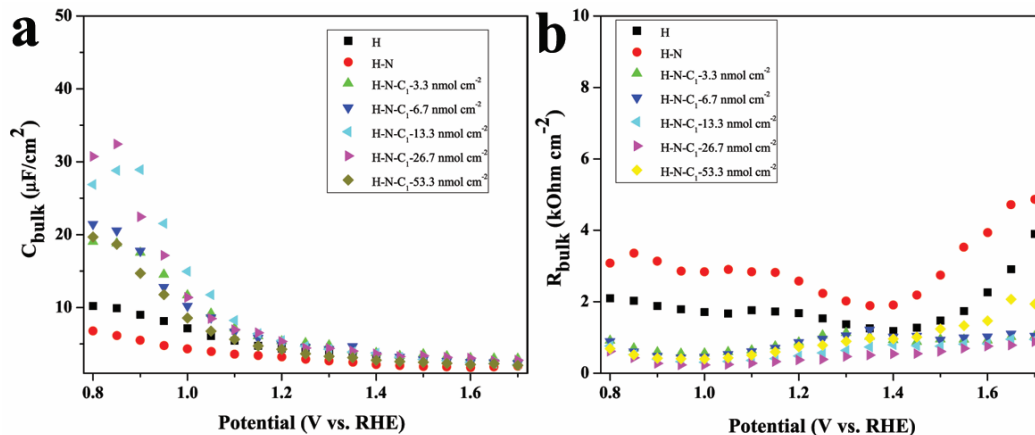


Figure S28. C_{bulk} (a) and R_{bulk} (b) values of C_1 loaded and bare hematite photoanodes fitted from impedance spectra measured under AM 1.5 G simulated sunlight at 100 mW cm^{-2} in 0.05 M borate buffer (pH 8.5) at different applied potentials. Experimental details: frequencies from 0.1 to 10000 Hz with 5 mV amplitude perturbation.

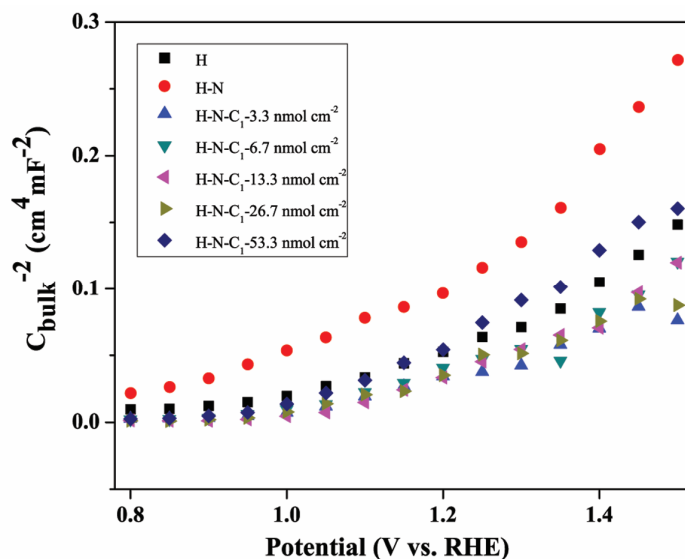


Figure S29. Mott-Schottky plots for C_1 loaded and bare hematite photoanodes derived from C_{bulk} values in Figure 28a.

8. (Photo)electrochemical characterization of C_2 loaded photoanodes

The fabrication of C_2 loaded hematite photoanodes was performed via same procedure as applied for C_1 . The same protocols were used for all (photo)electrochemical measurements and relevant data analyses.

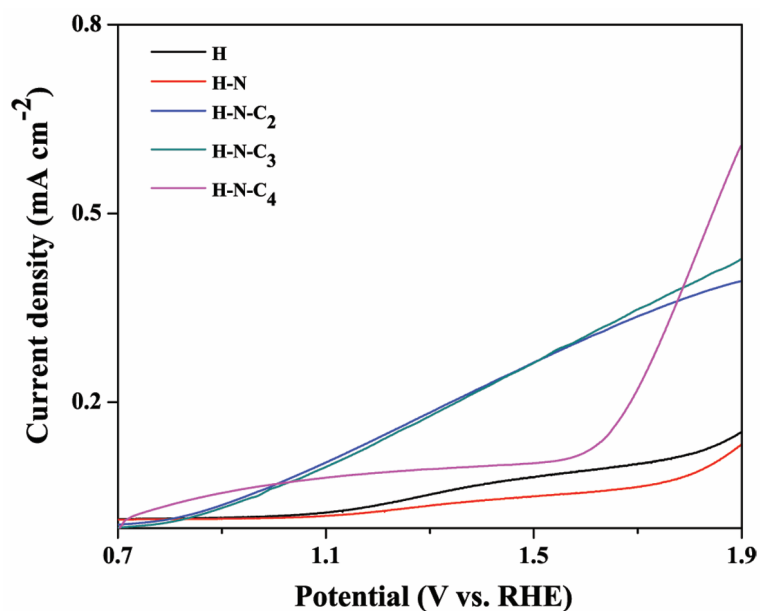


Figure S30. LSV curves of bare and different cocatalysts loaded photoanodes under AM 1.5 G simulated sunlight at 100 mW cm^{-2} in 0.05 M borate buffer (pH 8.5). Scan rate: 10 mV s^{-1} .

Table S1. Onset potential and current density comparison for different photoanodes

Samples	Onset potential (V vs. RHE)	Current density @ 1.23 V vs. RHE (mA cm^{-2})
H	1.04	0.04
H-N	1.12	0.02
H-N-C ₁	0.89	0.18
H-N-C ₂	0.83	0.16
H-N-C ₃	0.85	0.15
H-N-C ₄	0.73	0.10

a. TPS, IM-TPS and respective kinetic analysis

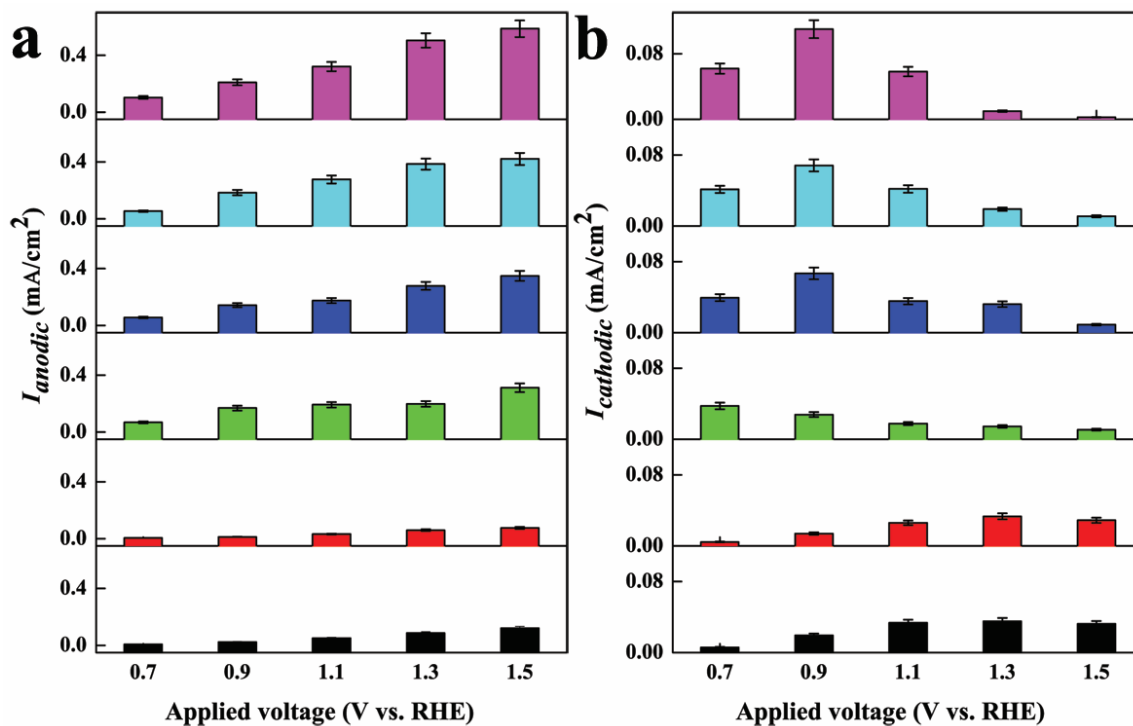


Figure S31. Transient current densities I_{anodic} (a) and $I_{cathodic}$ (b) for bare and C_2 loaded photoanodes (bottom to top: bare photoanode followed by C_2 modified photoanodes with increasing loading density from 0 to 53.3 nmol/cm²). Transient experiments were conducted at various constant biases vs. RHE in 0.05 M borate buffer (pH 8.5), and AM 1.5 G simulated sunlight at 100 mW cm⁻² was used for illumination. I_{anodic} and $I_{cathodic}$ values were the corresponding highest and lowest points recorded during anodic and cathodic transient process, and all lowest cathodic current densities were shown as positive values for easy comparison.

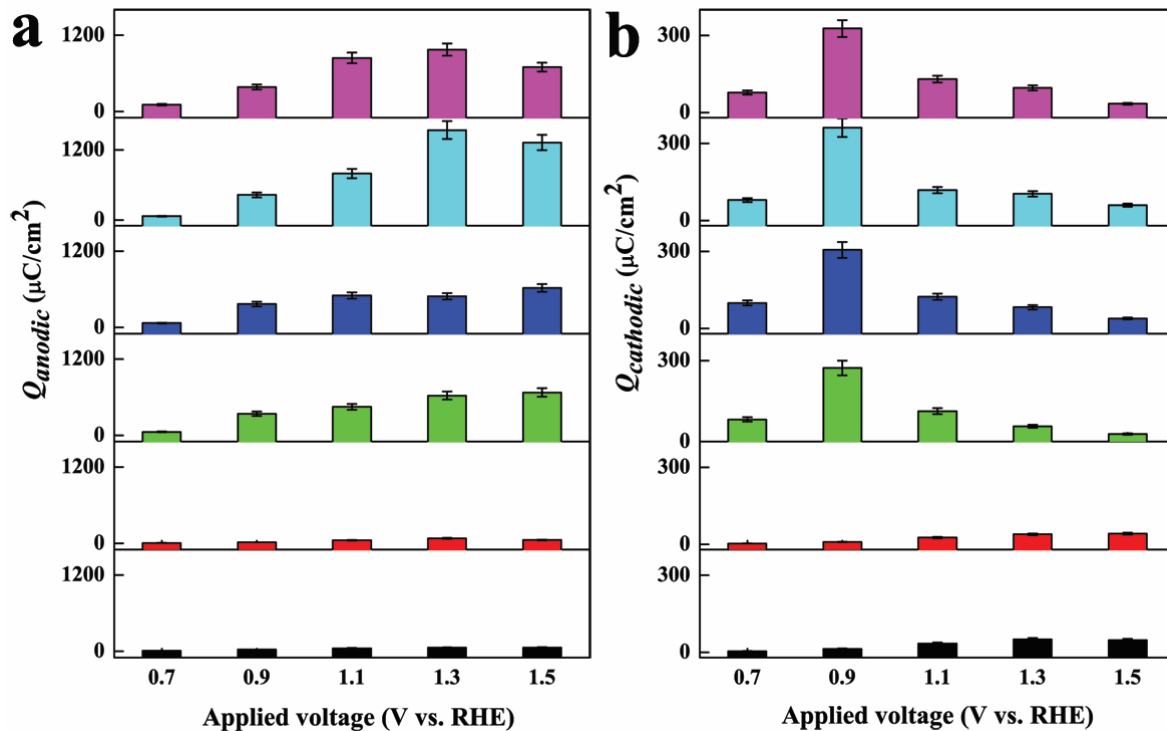


Figure S32. Transient Q_{anodic} (a) and $Q_{cathodic}$ (b) for bare and C_2 loaded photoanodes (bottom to top: bare photoanode, followed by C_2 modified photoanodes with increasing loading density from 0 to 53.3 nmol/cm²). Transient experiments were conducted at various constant biases vs. RHE in 0.05 M borate buffer (pH 8.5), and AM 1.5 G simulated sunlight at 100 mW cm⁻² was used for illumination. Q_{anodic} and $Q_{cathodic}$ were determined from integration of the current density curve over the time interval of the transient process using the built-in function of the Thales software.

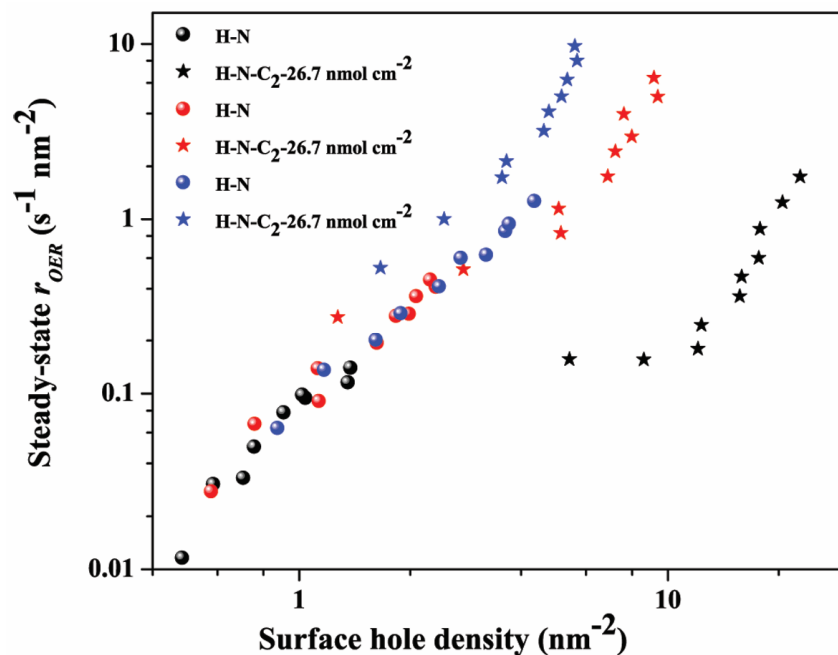


Figure S33. Rate law analysis of bare and C₂ loaded (26.7 nmol cm⁻²) photoanodes at 0.9, 1.1 and 1.3 V vs. RHE (black, red and blue color, respectively). Steady-state OER rates (r_{OER}) and surface hole densities were probed by IM-TPS.

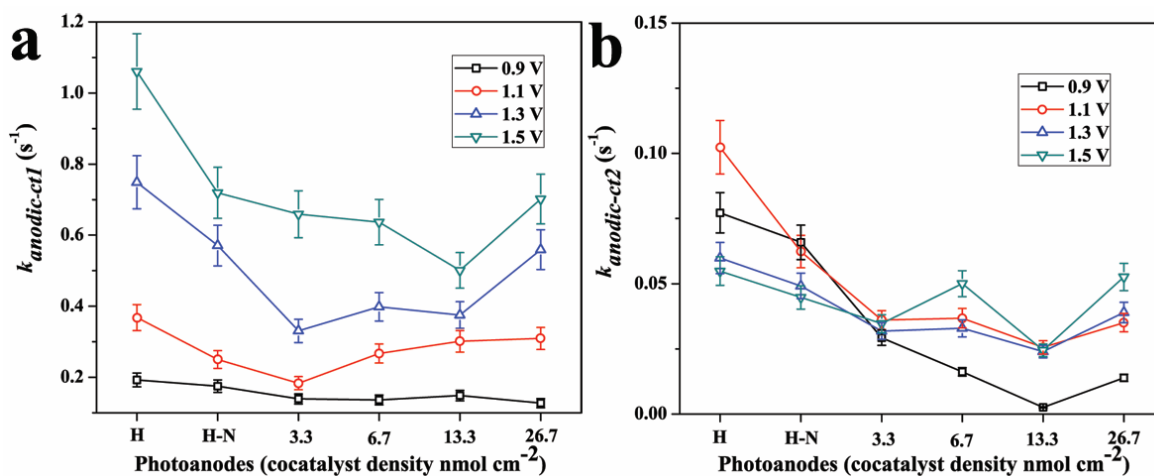


Figure S34. Comparison of the anodic forward hole accumulation/transfer rate constants for C₂ loaded and bare hematite photoanodes during the fast decay phase $k_{anodic-ct1}$ (a) and slow decay phase $k_{anodic-ct2}$ (b). The anodic transient process was initiated by exposing to one sun irradiation (100 mW/cm²) at constant applied biases vs. RHE, in 0.05 M borate buffer solution.

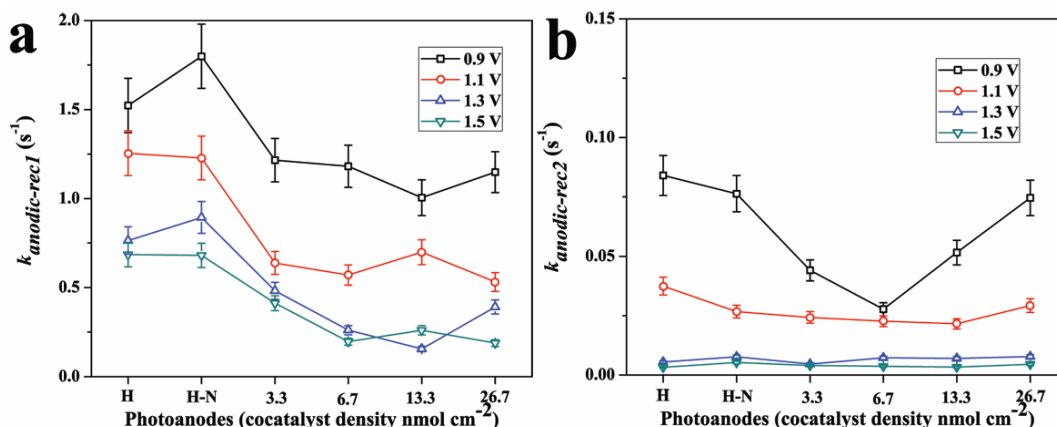


Figure S35. Comparison of the anodic back-electron hole recombination rate constants for C₂ loaded and bare hematite photoanodes during the fast decay phase $k_{anodic-rec1}$ (a) and slow decay phase $k_{anodic-rec2}$ (b). The anodic transient process was initiated by exposing to one sun irradiation (100 mW/cm²) at constant applied biases vs. RHE, in 0.05 M borate buffer solution.

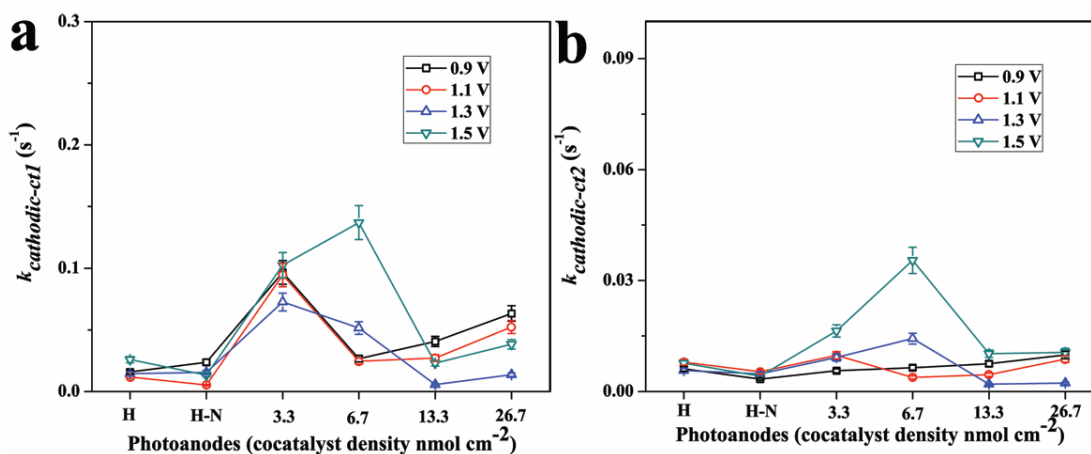


Figure S36. Comparison of the cathodic forward hole accumulation/transfer rate constants for C₂ loaded and bare hematite photoanodes during the fast decay phase $k_{anodic-ct1}$ (a) and slow decay phase $k_{anodic-ct2}$ (b). The anodic transient process was initiated by turning the light off at constant applied biases vs. RHE, in 0.05 M borate buffer solution.

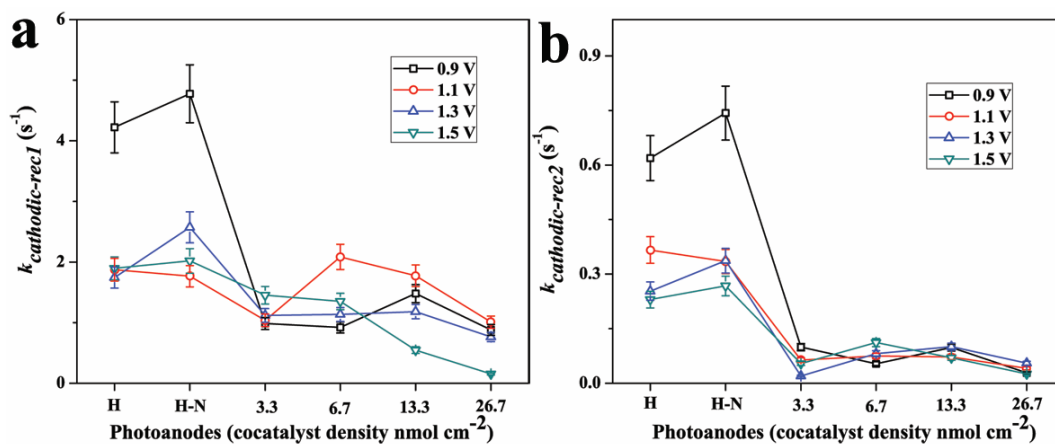


Figure S37. Comparison of the cathodic back-electron hole recombination rate constants for C_2 loaded and bare hematite photoanodes during the fast decay phase $k_{anodic-rec1}$ (a) and slow decay phase $k_{anodic-rec2}$ (b). The anodic transient process was initiated by turning the light off at constant applied biases vs. RHE, in 0.05 M borate buffer solution.

b. PEIS, IM-EIS and respective kinetic analysis

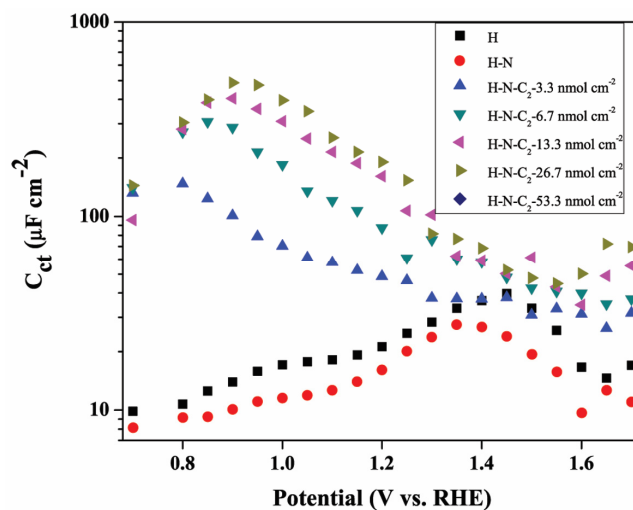


Figure S38. C_{ct} values of C_2 loaded and bare hematite photoanodes fitted from impedance spectra measured under AM 1.5 G simulated sunlight at 100 mW cm^{-2} in 0.05 M borate buffer (pH 8.5) at different applied potentials. Experimental details: frequency, 0.1 to 10000 Hz with 5 mV amplitude perturbation.

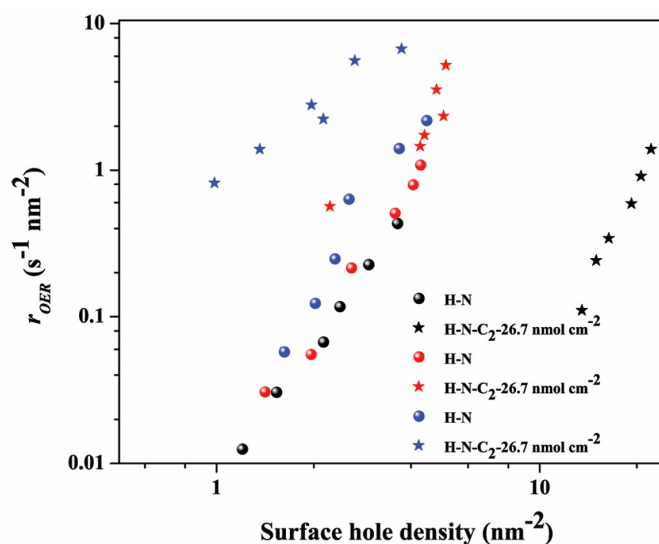


Figure S39. Rate law analysis of bare and C_2 loaded ($26.7 \text{ nmol cm}^{-2}$) photoanodes at 0.9, 1.1 and 1.3 V vs. RHE (black, red and blue color, respectively), r_{OER} and surface hole densities were probed by IM-EIS.

9. (Photo)electrochemical characterization of C₃ loaded photoanodes

The fabrication of C₃ loaded hematite photoanodes was performed via same procedure as applied for C₁. The same protocols were used for all (photo)electrochemical measurements and relevant data analyses.

a. TPS, IM-TPS and respective kinetic analysis

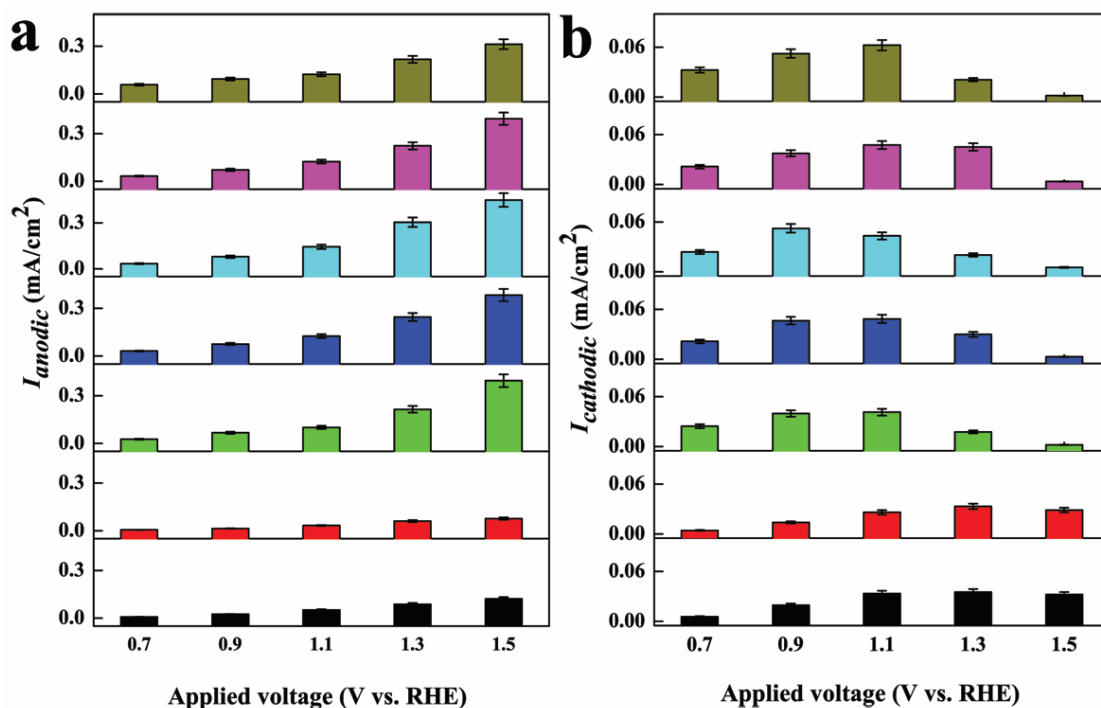


Figure S40. Transient I_{anodic} (a) and $I_{cathodic}$ (b) for bare and C₃ loaded photoanodes (bottom to top: bare photoanode, followed by C₃ modified photoanodes with increasing loading density from 0 to 53.3 nmol cm⁻²). Transient experiments were conducted at various constant biases vs. RHE in 0.05 M borate buffer (pH 8.5); AM 1.5 G simulated sunlight at 100 mW cm⁻² was used for illumination. I_{anodic} and $I_{cathodic}$ values were corresponding to the highest and lowest points recorded during the anodic and cathodic transient process, and all cathodic lowest current densities were shown as positive values to facilitate comparisons.

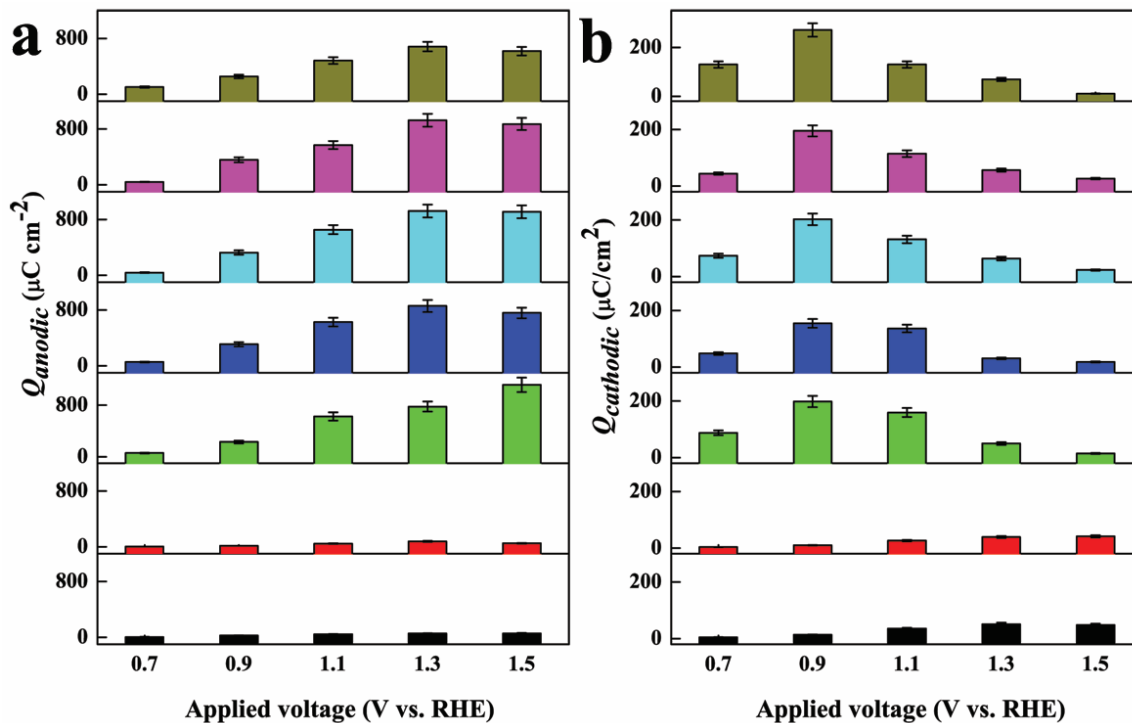


Figure S41. Transient Q_{anodic} (a) and $Q_{cathodic}$ (b) for bare and C_3 loaded photoanodes (bottom to top: bare photoanode, followed by C_3 modified photoanodes with increasing loading density from 0 to 53.3 nmol cm^{-2}). Transient experiments were conducted at various constant biases vs. RHE in 0.05 M borate buffer (pH 8.5); AM 1.5 G simulated sunlight at 100 mW cm^{-2} was used for illumination; calculation of Q_{anodic} and $Q_{cathodic}$ was done by integration of the current density curve over the time interval of the transient process using the built-in function of the Thales software.

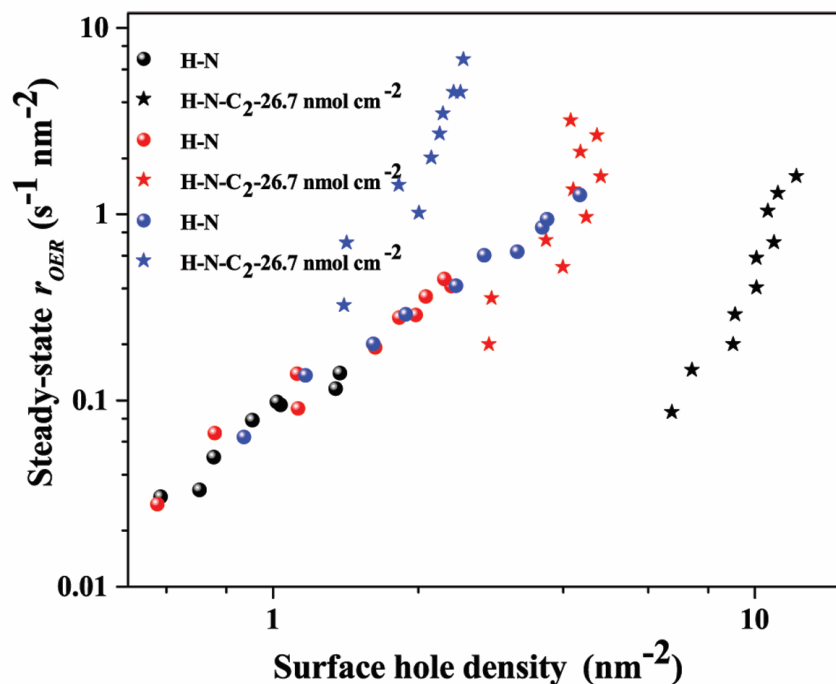


Figure S42. Rate law analysis of bare and C₃ loaded (26.7 nmol cm⁻²) photoanodes at 0.9, 1.1 and 1.3 V vs. RHE (black, red and blue color, respectively). Steady-state OER rates (r_{OER}) and surface hole densities were probed by IM-TPS.

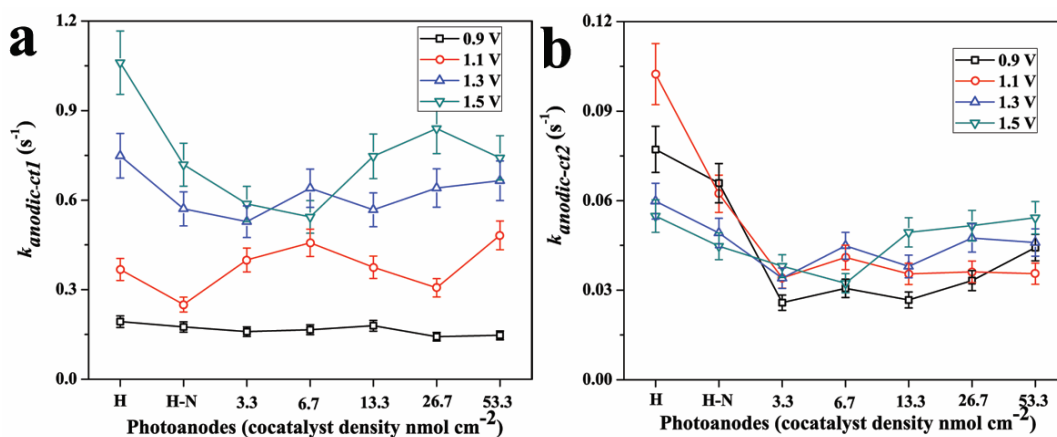


Figure S43. Comparison of the anodic forward hole accumulation/transfer rate constants for C₃ loaded and bare hematite photoanodes during the fast decay phase $k_{anodic-ct1}$ (a) and slow decay phase $k_{anodic-ct2}$ (b). The anodic transient process was initiated by exposing to one sun irradiation (100 mW cm⁻²) at constant applied biases vs. RHE, in 0.05 M borate buffer solution.

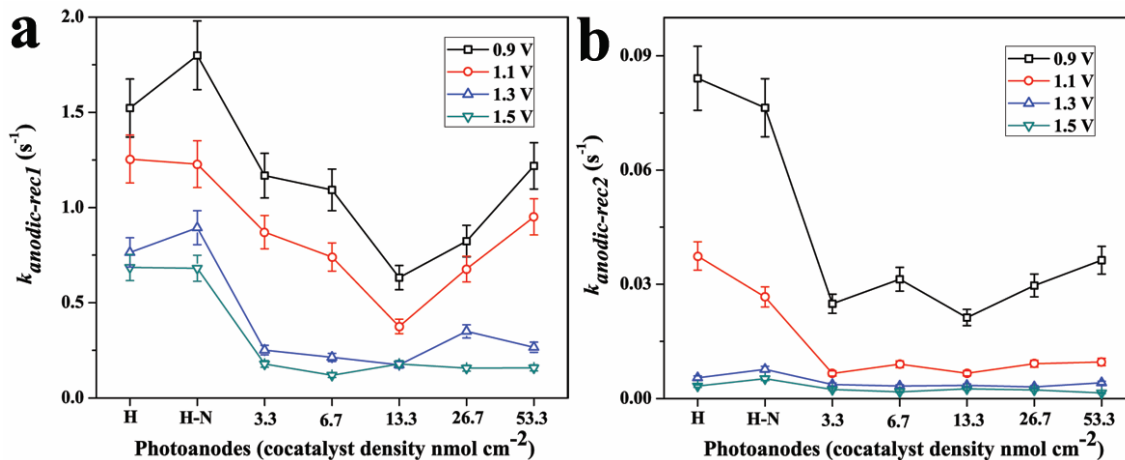


Figure S44. Comparison of the anodic back-electron hole recombination rate constants for C₃ loaded and bare hematite photoanodes during the fast decay phase $k_{\text{anodic-rec1}}$ (a) and slow decay phase $k_{\text{anodic-rec2}}$ (b). The anodic transient process was initiated by exposing to one sun irradiation (100 mW cm⁻²) at constant applied biases vs. RHE, in 0.05 M borate buffer solution.

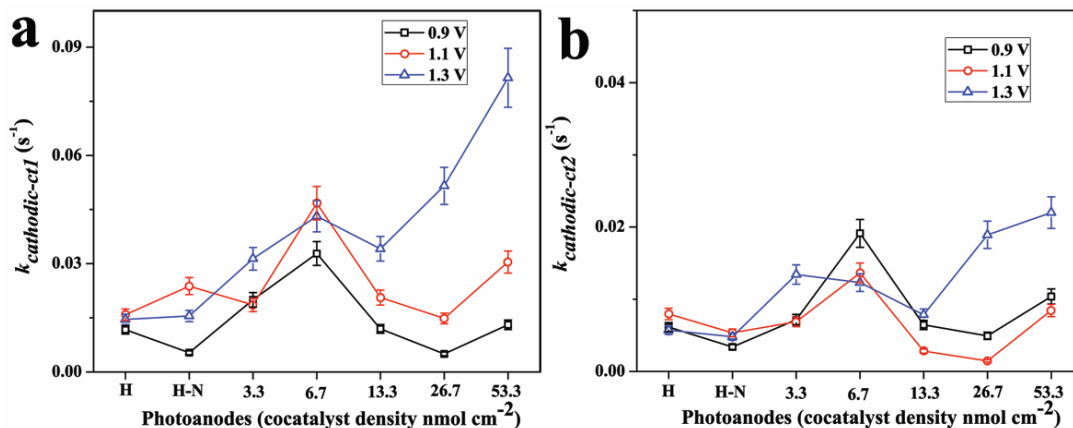


Figure S45. Comparison of the cathodic forward hole accumulation/transfer rate constants for C₃ loaded and bare hematite photoanodes during the fast decay phase $k_{\text{anodic-ct1}}$ (a) and slow decay phase $k_{\text{anodic-ct2}}$ (b). The anodic transient process was initiated by turning the light off at constant applied biases vs. RHE, in 0.05 M borate buffer solution.

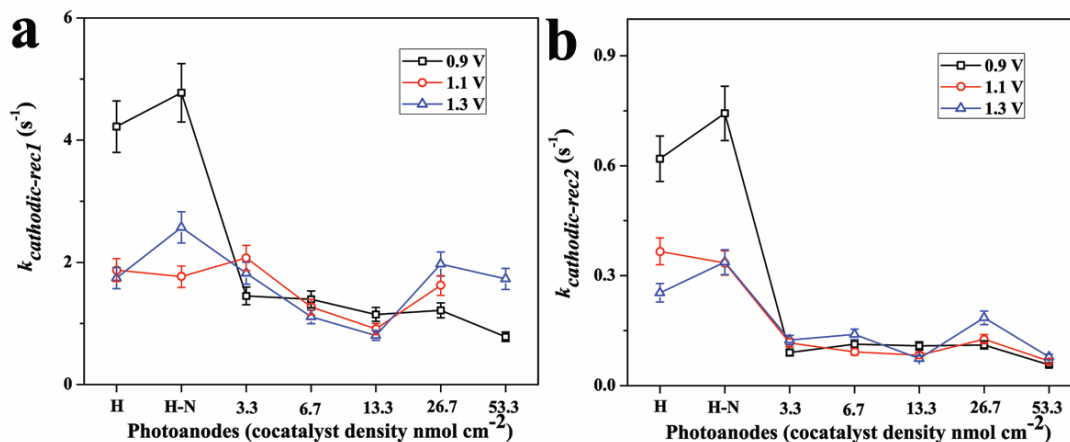


Figure S46. Comparison of the cathodic back-electron hole recombination rate constants for C₃ loaded and bare hematite photoanodes during the fast decay phase $k_{\text{anodic-rec1}}$ (a) and slow decay phase $k_{\text{anodic-rec2}}$ (b). The anodic transient process was initiated by turning the light off at constant applied biases vs. RHE, in 0.05 M borate buffer solution.

b. PEIS, IM-EIS and respective kinetic analysis

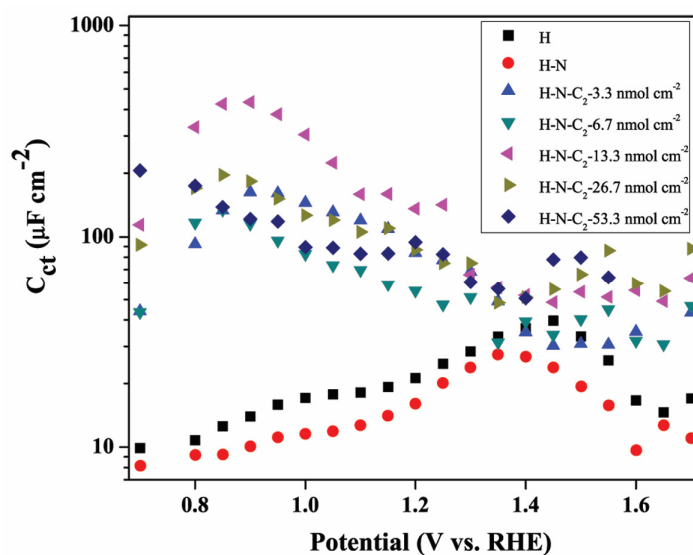


Figure S47. C_{ct} values of C₃ loaded and bare hematite photoanodes fitted from impedance spectra measured under AM 1.5 G simulated sunlight at 100 mW cm⁻² in 0.05 M borate buffer (pH 8.5) at different applied potentials. Experimental details: frequencies from 0.1 to 10000 Hz with 5 mV amplitude perturbation.

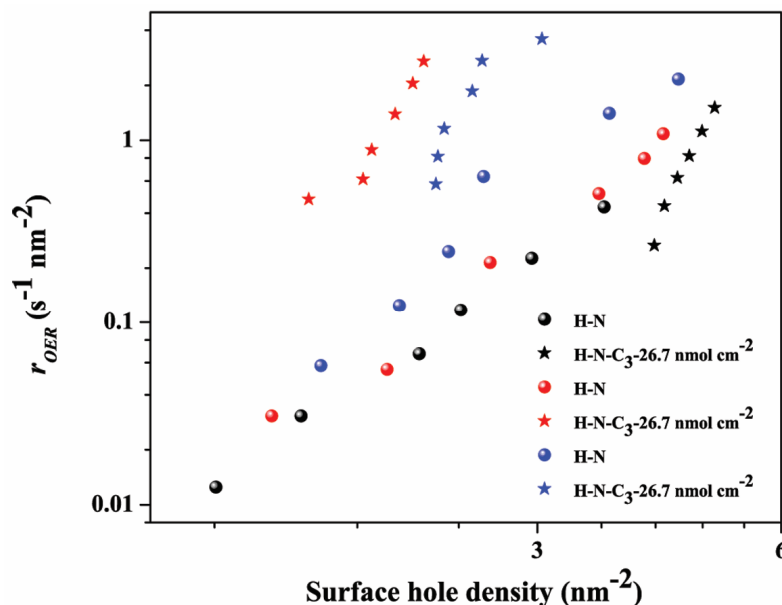


Figure S48. Rate law analysis of bare and C₃ loaded (26.7 nmol cm⁻²) photoanodes at 0.9 and 1.1 V vs. RHE (black and red color, respectively), r_{OER} and surface hole densities were probed by IM-EIS.

10. (Photo)electrochemical measurement of C₄ loaded photoanodes

C₄ was deposited by spin coating on freshly prepared and screened hematite photoanodes using a previously reported method.¹⁴ Freshly prepared cobalt nitrate hexahydrate solution (5 mM) was used as precursor, and approximately 0.25 mL of this precursor solution was added to the hematite surface, followed by spinning at 3000 rpm for one minute. Subsequently, the obtained samples were annealed in a preheated furnace (100 °C) in air for one hour. To change the amount of C₄ loading, the deposition process was repeated over different cycles. All (photo)electrochemical measurements and relevant data analyses were performed with the the same procedures as applied for C₁.

a. TPS, IM-TPS and respective kinetic analysis

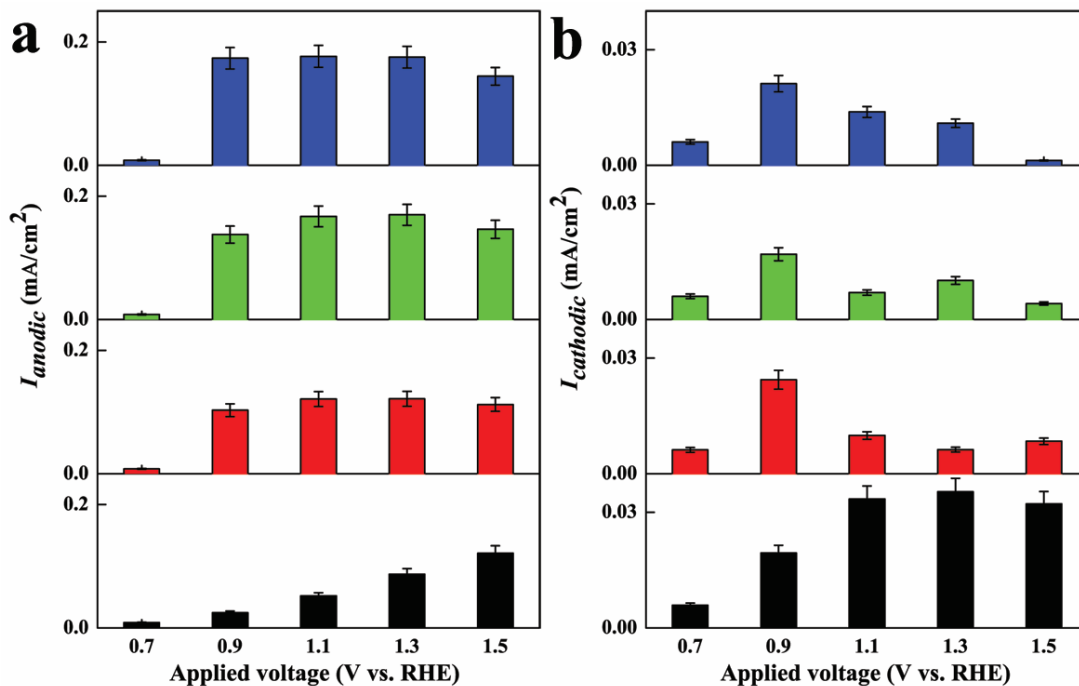


Figure S49. Transient I_{anodic} (a) and $I_{cathodic}$ (b) for bare and C₄ loaded photoanodes (bottom to top: bare photoanode, followed by C₄ modified photoanodes with loading cycles increasing from 1 to 4). Transient experiments were conducted at various constant biases vs. RHE in 0.05 M borate buffer (pH 8.5); AM 1.5 G simulated sunlight at 100 mW cm⁻² was used for illumination. I_{anodic} and $I_{cathodic}$ values were derived from the corresponding highest and lowest points recorded during anodic and cathodic transient processes, and all cathodic lowest current densities are represented as positive values to facilitate comparisons.

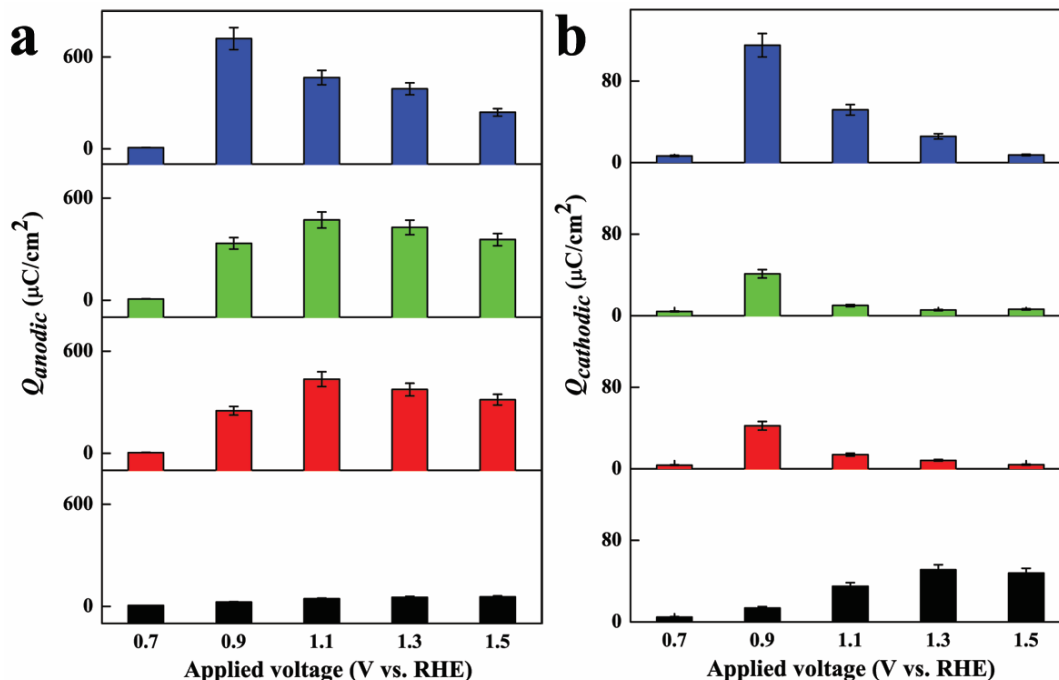


Figure S50. Transient Q_{anodic} (a) and $Q_{cathodic}$ (b) for bare and C_4 loaded photoanodes (bottom to top: bare photoanode, followed by C_4 modified photoanodes with loading cycles increasing from 1 to 4). Transient experiments were conducted at various constant biases vs. RHE in 0.05 M borate buffer (pH 8.5); AM 1.5 G simulated sunlight at 100 mW cm^{-2} was used for illumination; Q_{anodic} and $Q_{cathodic}$ were calculated from integration of the current density curve over the time interval of the transient process using the built-in function of the Thales software.

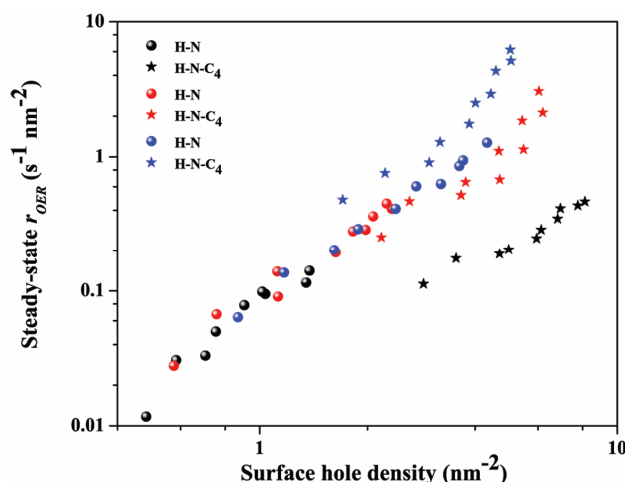


Figure S51. Rate law analysis of bare and C_4 loaded photoanodes at 0.9, 1.1 and 1.3 V vs. RHE (black, red and blue color, respectively), steady-state OER rates (r_{OER}) and surface hole densities were probed by IM-TPS.

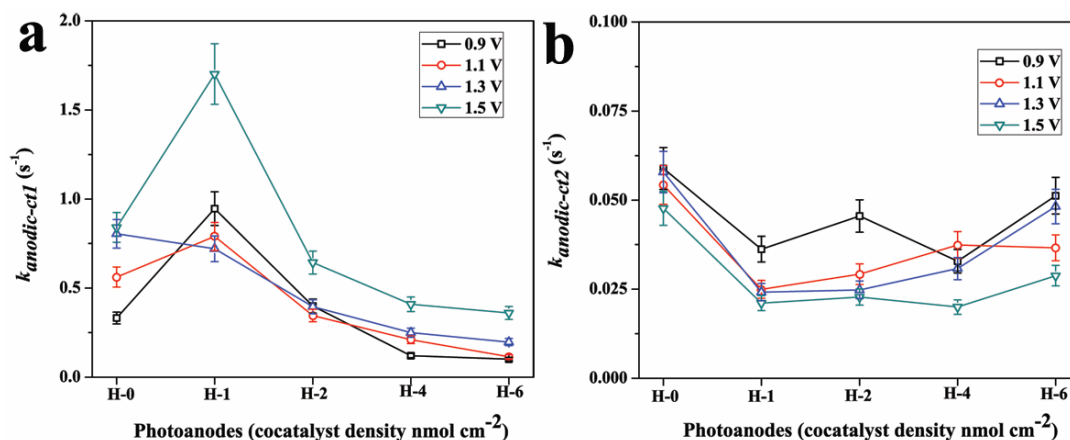


Figure S52. Comparison of the anodic forward hole accumulation/transfer rate constants for C₄ loaded and bare hematite photoanodes during the fast decay phase $k_{anodic-ct1}$ (a) and slow decay phase $k_{anodic-ct2}$ (b). The anodic transient process was initiated by exposing to one sun irradiation (100 mW cm⁻²) at constant applied biases vs. RHE, in 0.05 M borate buffer solution.

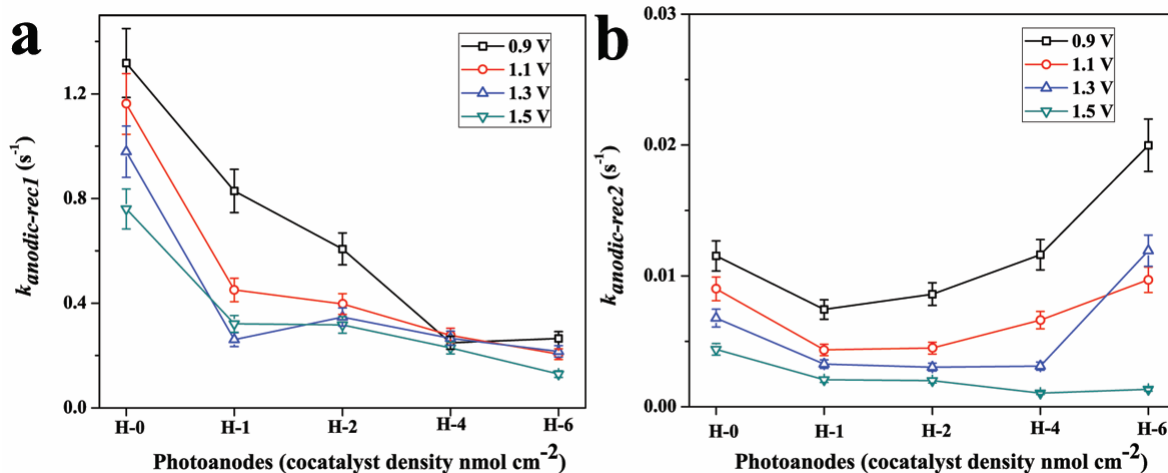


Figure S53. Comparison of the anodic back-electron hole recombination rate constants for C₄ loaded and bare hematite photoanodes during the fast decay phase $k_{anodic-rec1}$ (a) and slow decay phase $k_{anodic-rec2}$ (b). The anodic transient process was initiated by exposing to one sun irradiation (100 mW cm⁻²) at constant applied biases vs. RHE, in 0.05 M borate buffer solution.

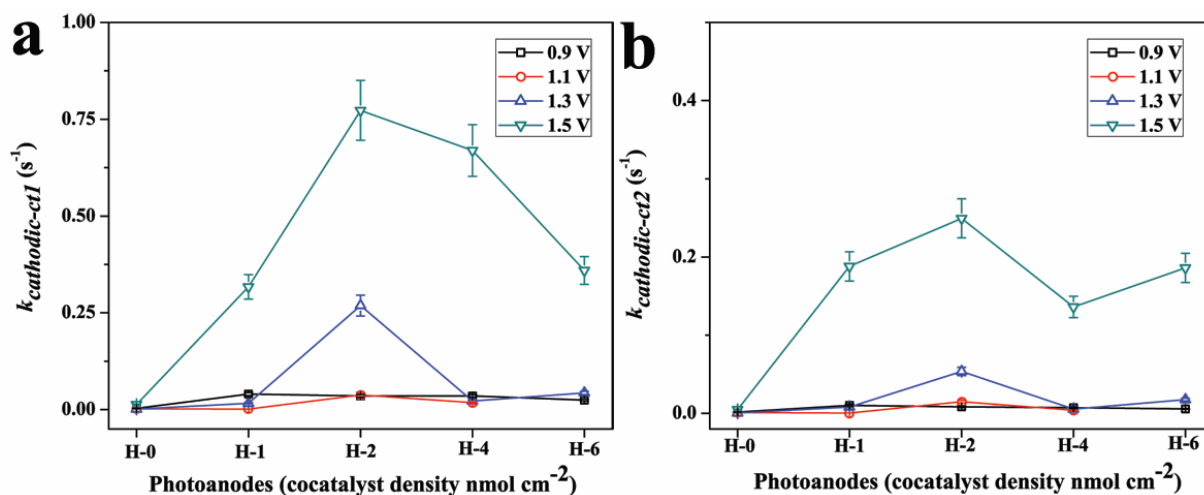


Figure S54. Comparison of the cathodic forward hole accumulation/transfer rate constants for C₄ loaded and bare hematite photoanodes during the fast decay phase $k_{\text{cathodic-ct1}}$ (a) and slow decay phase $k_{\text{cathodic-ct2}}$ (b). The anodic transient process was initiated by turning light off at constant applied biases vs. RHE, in 0.05 M borate buffer solution.

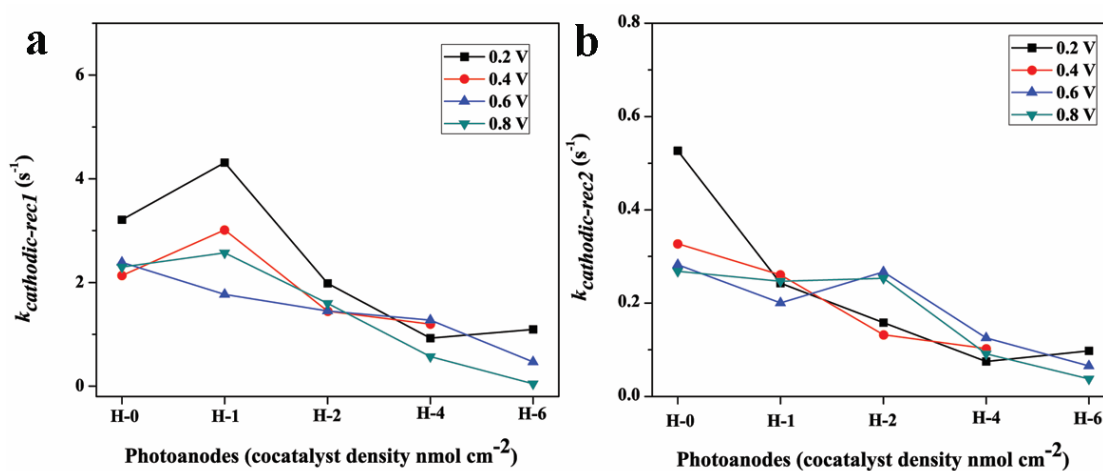


Figure S55. Comparison of the cathodic back-electron hole recombination rate constants for C₄ loaded and bare hematite photoanodes during the fast decay phase $k_{\text{cathodic-rec1}}$ (a) and slow decay phase $k_{\text{cathodic-rec2}}$ (b). The anodic transient process was initiated by turning light off at constant applied biases vs. RHE, in 0.05 M borate buffer solution.

b. PEIS, IM-EIS and respective kinetic analysis

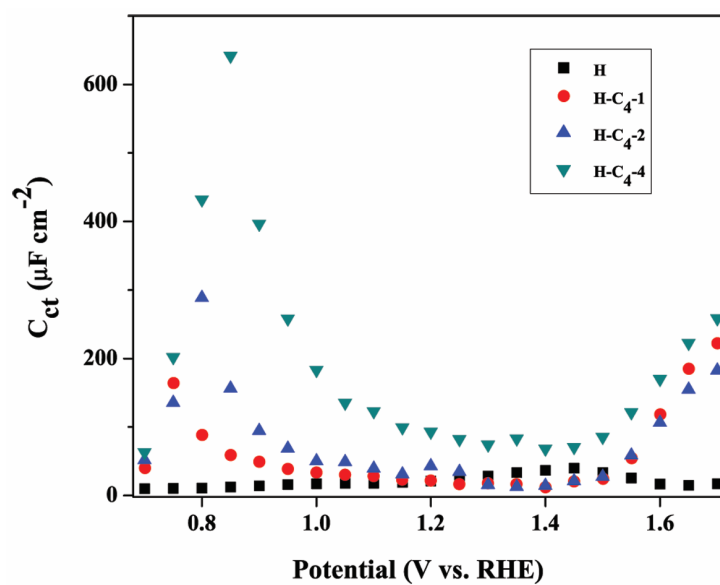


Figure S56. C_{ct} values of C₄ loaded and bare hematite photoanodes fitted from impedance spectra measured under AM 1.5 G simulated sunlight at 100 mW cm⁻² in 0.05 M borate buffer (pH 8.5) at different applied potentials. Experimental details: frequencies from 0.1 to 10000 Hz with 5 mV amplitude perturbation.

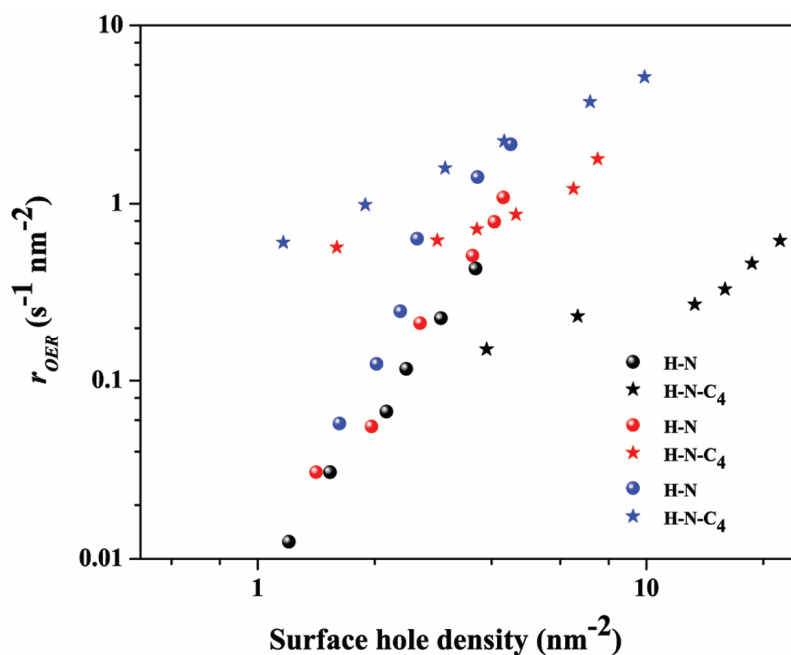


Figure S57. Rate law analysis of bare and C₄ loaded photoanodes at 0.9, 1.1 and 1.3 V vs. RHE (black, red and blue color, respectively), r_{OER} and surface hole densities were probed by IM-EIS.

11. Stability characterization of molecular cocatalysts modified photoanode

a. (Photo)electrochemical study

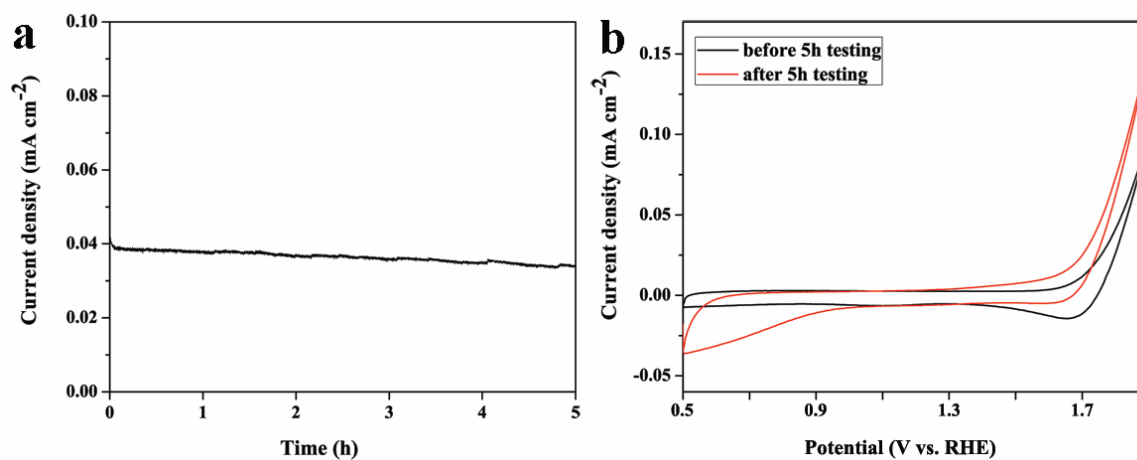


Figure S58. Controlled potential photoelectrolysis at 1.3 V vs. RHE (a) and CV before and after stability tests (b) of Nafion modified hematite photoanode in 0.05 M borate buffer (pH 8.5). AM 1.5 G simulated sunlight at 100 mW cm⁻² was used as light source.

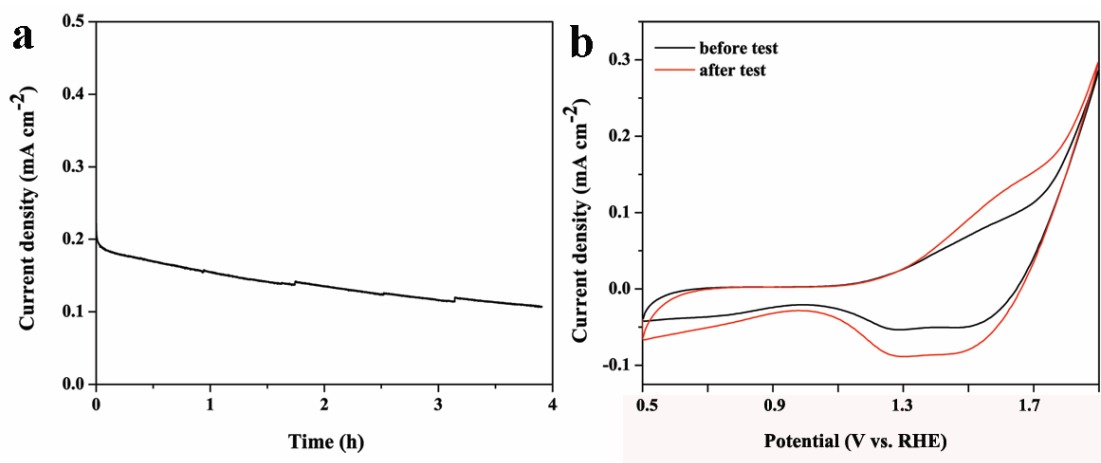


Figure S59. Controlled potential photoelectrolysis at 1.3 V vs. RHE (a) and CV before and after stability tests (b) of C₁ modified hematite photoanode (26.7 nmol cm⁻²) in 0.05 M borate buffer (pH 8.5). AM 1.5 G simulated sunlight at 100 mW cm⁻² was used as light source.

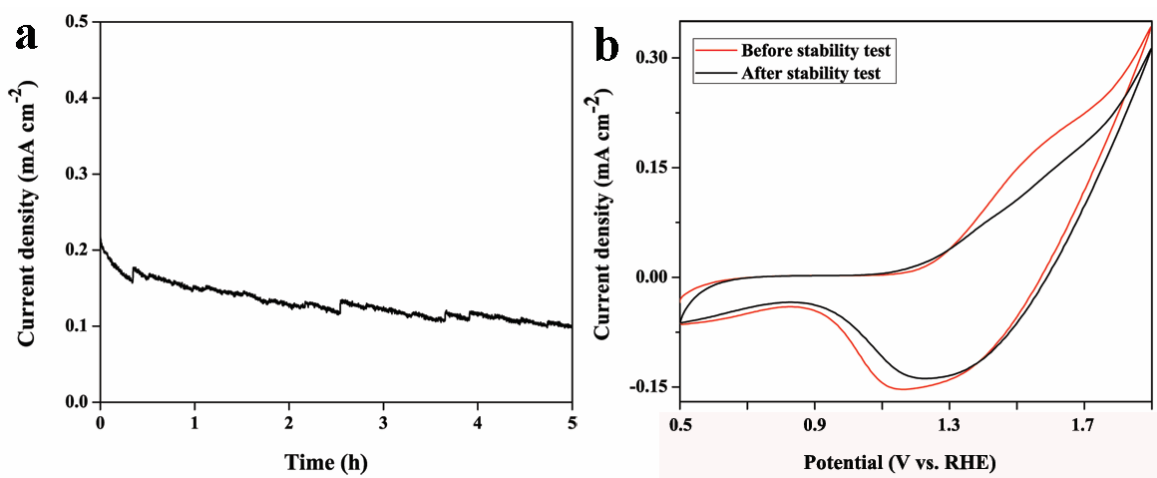


Figure S60. Controlled potential photoelectrolysis at 1.3 V vs. RHE (a) and CV before and after stability tests (b) of C₂ modified hematite photoanode (26.7 nmol cm⁻²) in 0.05 M borate buffer (pH 8.5). AM 1.5 G simulated sunlight at 100 mW cm⁻² was used as light source.

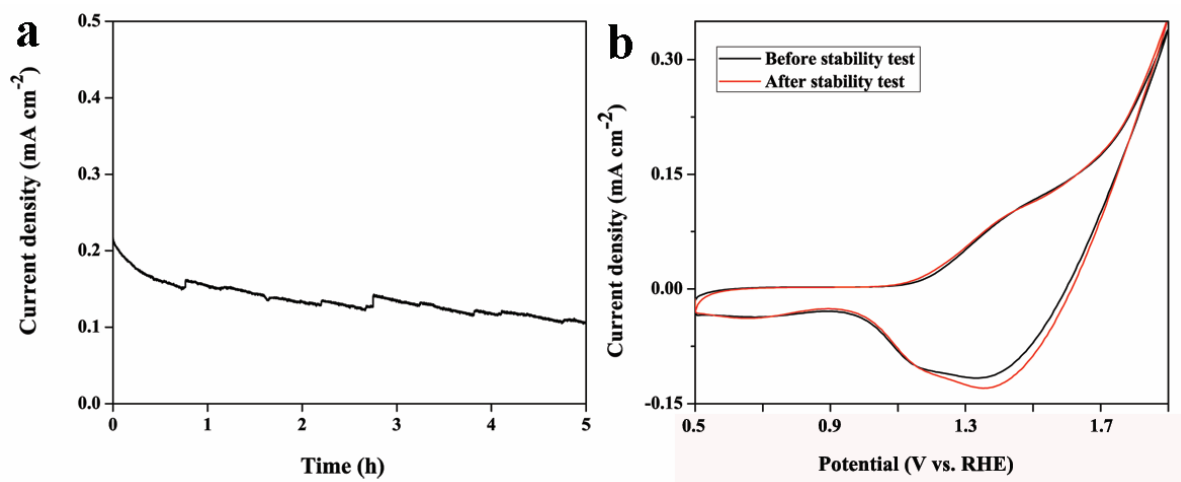


Figure S61. Controlled potential photoelectrolysis at 1.3 V vs. RHE (a) and CV before and after stability tests (b) of C_3 ($26.7 \text{ nmol cm}^{-2}$) modified hematite photoanode in 0.05 M borate buffer (pH 8.5). AM 1.5 G simulated sunlight at 100 mW cm^{-2} was used as light source.



Figure S62. Image of photoelectrochemical cell after controlled potential photoelectrolysis at 1.3 V vs. RHE with C_1 loaded photoanode inside ($26.7 \text{ nmol cm}^{-2}$).

b. HAADF-STEM studies

Aberration-corrected scanning transmission electron microscopy (STEM) was performed on a Titan Themis microscope operated at 300 kV in the high angle annular dark field (HAADF) mode.

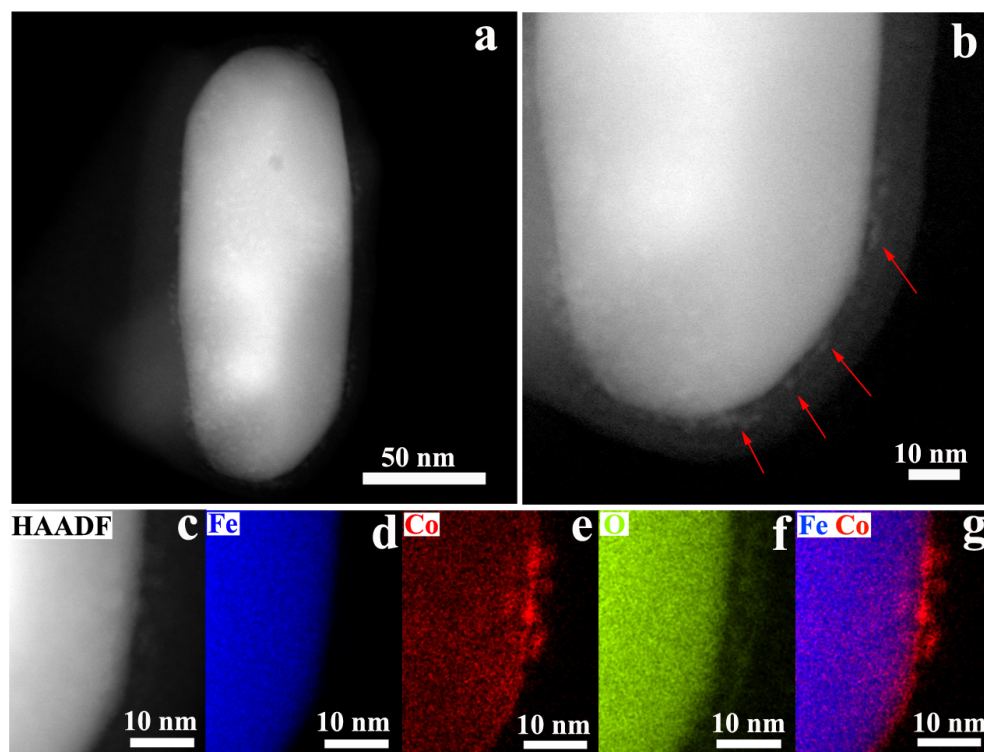


Figure S63. STEM-HAADF analysis of the newly formed species on hematite surface after aging at 1.7 V vs RHE (a), magnified image (b), and selected area EDX images of (c) HAADF, (d) Fe, (d) Co, (f) O, (g) Fe and Co.

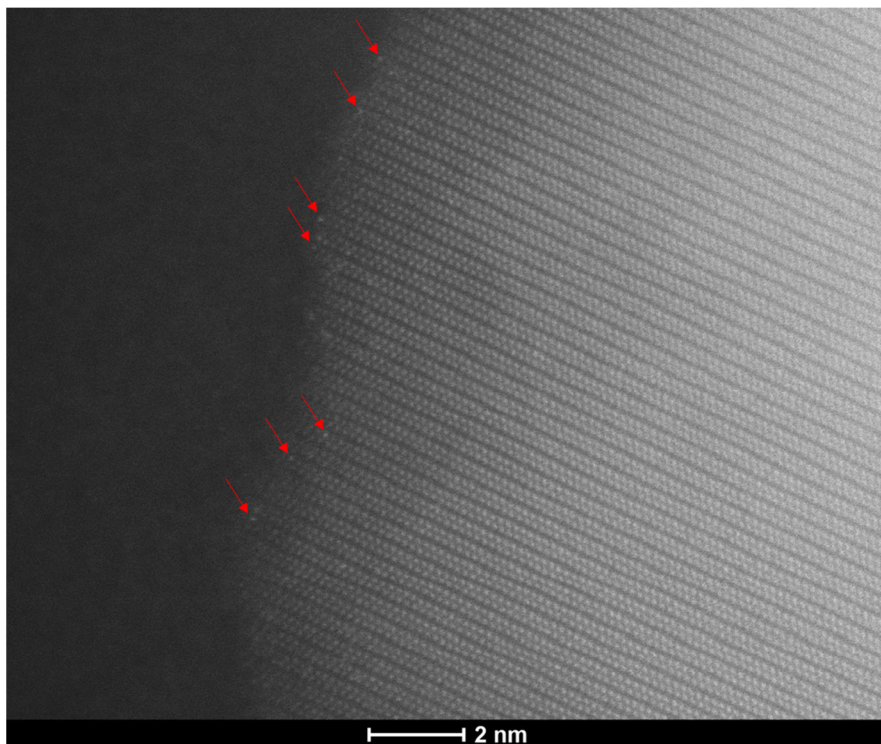


Figure S64. STEM-HAADF image with atomic resolution indicating the existence of single atoms or molecular species on the hematite surface after aging at 1.7 V vs RHE.

Some single atoms or molecular species can also be identified on the hematite surface (**Fig. S66**), which means that the transformation of molecular cocatalysts to clusters is a kinetically controlled process.

c. X-ray photoelectron spectroscopy (XPS) studies

XPS spectroscopy was performed in an ultra-high vacuum system at normal emission using an achromatic twin anode X-ray source (Si, Mg) operated at 280 W and a hemispherical electron analyzer equipped with 6-channeltron detectors. Four different samples were investigated: i) freshly prepared C₁ loaded photoanode, ii) C₁ loaded photoanode after aging at 1.3 V, iii) C₁ loaded photoanode after aging at 1.7 V vs RHE for 2 h, iv) CoO_x loaded photoanode (CoO_x was prepared via electrodeposition). The aging was carried out in the photoelectrochemical cell with photoanode used as working electrode, Pt wire as counter electrode and Ag/AgCl (in saturated KCl) as reference electrode, and AM 1.5 G simulated sunlight at 100 mW cm⁻² was used as light source. For a better comparison, the as prepared sample was offsetted on the binding energy scale to allow a quantitative comparison among spectra. The sample charging was verified by using a Si anode that showed smaller charging due to the lower X-ray flux (-5.08 eV for C1s, since it was not overlapping with any Auger peaks).

In addition to the two main regions of the Co 2p ($2p_{3/2}$, 784.2 eV and $2p_{1/2}$, 799.6 eV) core-level spectrum obtained from the freshly prepared photoanode with molecular cocatalysts (**Fig. S68a**), two shoulder peaks with lower binding energy ($2p_{3/2}$, at 781.0 eV and $2p_{1/2}$, at 796.2 eV) increase slightly after aging at 1.3 V vs. RHE (**Fig. S68b**) and become dominant after aging at higher bias (**Fig. S68c**). Both emerging peaks originate from the newly formed CoO_x species as evidenced by the spectrum recorded with as-prepared CoO_x (**Fig. S68d**).

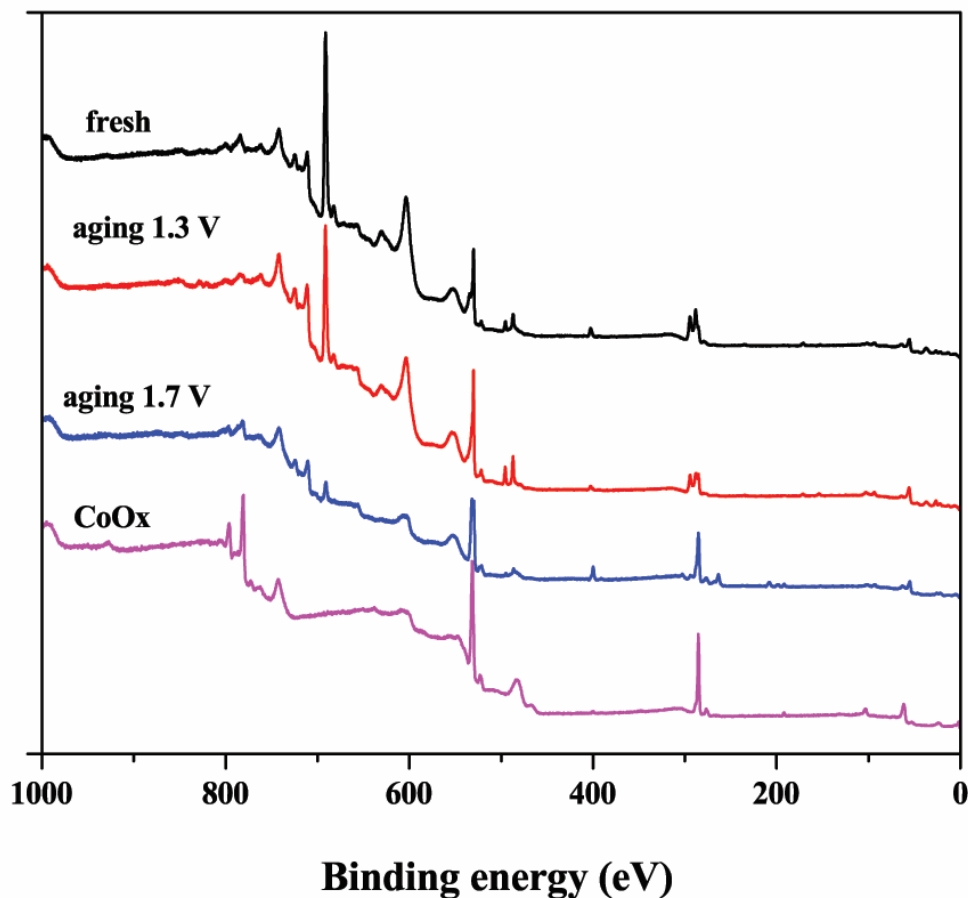


Figure S65. XPS survey spectrum of freshly prepared C_1 loaded photoanode and after aging at 1.3 V and 1.7 V vs RHE for 2 h, and of a CoO_x loaded photoanode. Spectra were acquired at normal emission using Mg K_α radiation.

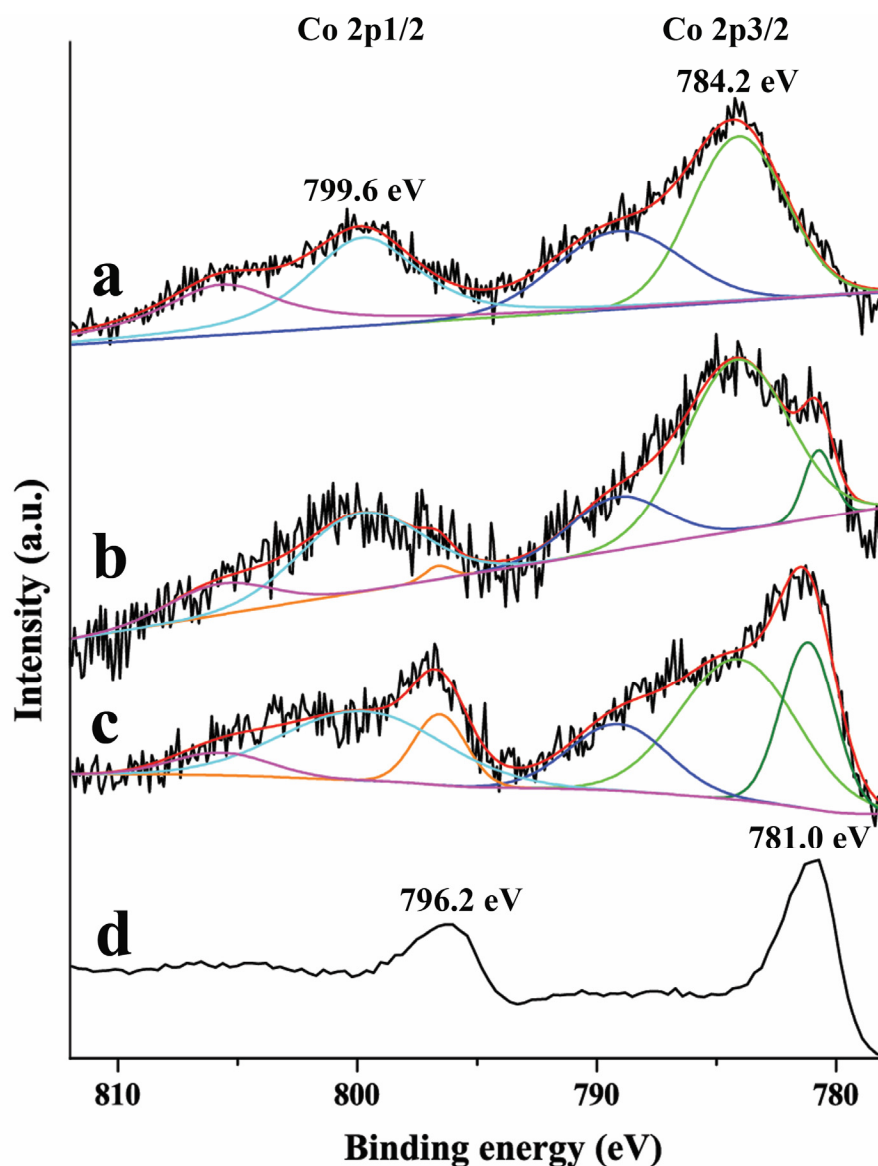


Figure S66. The Co₂p XPS spectra of (a) freshly prepared C₁ loaded photoanode (b) after aging at 1.3 V (c) 1.7 V vs RHE for 2 h, and (d) CoO_x loaded photoanode.

d. Stability discussions

A close examination of the (photo)electrochemical data (Figure S26, Table S1) indicates that electrodes modified with molecular and heterogeneous cocatalysts have distinct onset potentials and PEC behaviors, which are determined by different electronic properties of active centers. This is also supported by TPS and PEIS analysis, for example, Q_{anodic} and C_{ct} maximized between 1.0 V vs. RHE for C₁ modified electrode,

while it was 0.85 V vs. RHE for CoO_x. This slight voltage difference (0.15 V) strongly points out that most of C₁ still preserves its molecular nature during data acquisition.

Third, identification of the small amount of particulate species that originate from the molecular cocatalyst is very challenging, even for systems that operate in liquid phase. Therefore, to obtain full information of the molecular identity on solid surfaces, operando techniques, like ambient pressure X-ray photoelectron spectroscopy (AP-XPS), which probes the material interfaces with high sensitivity, are essential and projected for follow-up studies. Even though molecular cocatalysts may not retain their identity under longer operational conditions, they still have great potential as tunable precursors for more sophisticated nanoscale cocatalyst design.

For the cocatalysts-photoanode system, these surface loaded active species will compete with photoanode surface states for hole storage, transfer and recombination. Understanding the dynamics of this inter-related multiple process is the key to resolve the long-standing problem of fully explaining cocatalysts in a quantitative manner. Thus, to draw a full picture of this complicated system, a combination of multiple operando techniques is essential. Such as (i) ultrafast TAS which probes the photo-generated holes at femtosecond to second resolution, (ii) (photo)electrochemical analysis that tracks the dynamics of electrons, (iii) DWE operation geometry that detects the electronic differences of materials interfaces, and (iv) surface sensitive techniques (AFM, AP-XPS, Raman, FTIR) etc.

References

- (1) Kment, S.; Riboni, F.; Pausova, S.; Wang, L.; Wang, L.; Han, H.; Hubicka, Z.; Krysa, J.; Schmuki, P.; Zboril, R. Photoanodes based on TiO₂ and α -Fe₂O₃ for solar water splitting - superior role of 1D nanoarchitectures and of combined heterostructures. *Chem. Soc. Rev.* **2017**, *46*, 3716–3769, DOI: 10.1039/c6cs00015k.
- (2) Wang, D.; Chang, G.; Zhang, Y.; Chao, J.; Yang, J.; Su, S.; Wang, L.; Fan, C.; Wang, L. Hierarchical three-dimensional branched hematite nanorod arrays with enhanced mid-visible light absorption for high-efficiency photoelectrochemical water splitting. *Nanoscale* **2016**, *8*, 12697–12701, DOI: 10.1039/c6nr03855g.
- (3) Zandi, O.; Hamann, T. W. Enhanced Water Splitting Efficiency Through Selective Surface State Removal. *J. Phys. Chem. Lett.* **2014**, *5*, 1522–1526, DOI: 10.1021/jz500535a.
- (4) Sivula, K.; Zboril, R.; Le Formal, F.; Robert, R.; Weidenkaff, A.; Tucek, J.; Frydrych, J.; Grätzel, M. Photoelectrochemical water splitting with mesoporous hematite prepared by a solution-based colloidal approach. *J. Am. Chem. Soc.* **2010**, *132*, 7436–7444, DOI: 10.1021/ja101564f.
- (5) Song, F.; Moré, R.; Schilling, M.; Smolentsev, G.; Azzaroli, N.; Fox, T.; Lubner, S.; Patzke, G. R. {Co₄O₄} and {Co_xNi_{4-x}O₄} Cubane Water Oxidation Catalysts as Surface Cut-Outs of Cobalt Oxides. *J. Am. Chem. Soc.* **2017**, *139*, 14198–14208, DOI: 10.1021/jacs.7b07361.

- (6) Evangelisti, F.; More, R.; Hodel, F.; Lubner, S.; Patzke, G. R. 3d-4f {Co(II)3Ln(OR)4} Cubanes as Bio-Inspired Water Oxidation Catalysts. *J. Am. Chem. Soc.* **2015**, *137*, 11076–11084, DOI: 10.1021/jacs.5b05831.
- (7) Evangelisti, F.; Guttinger, R.; More, R.; Lubner, S.; Patzke, G. R. Closer to photosystem II: A Co₄O₄ cubane catalyst with flexible ligand architecture. *J. Am. Chem. Soc.* **2013**, *135*, 18734–18737, DOI: 10.1021/ja4098302.
- (8) Le Formal, F.; Pendlebury, S. R.; Cornuz, M.; Tilley, S. D.; Grätzel, M.; Durrant, J. R. Back electron-hole recombination in hematite photoanodes for water splitting. *J. Am. Chem. Soc.* **2014**, *136*, 2564–2574, DOI: 10.1021/ja412058x.
- (9) Kecsenovity, E.; Endrődi, B.; Tóth, P. S.; Zou, Y.; Dryfe, R. A. W.; Rajeshwar, K.; Janáky, C. Enhanced Photoelectrochemical Performance of Cuprous Oxide/Graphene Nanohybrids. *J. Am. Chem. Soc.* **2017**, *139*, 6682–6692, DOI: 10.1021/jacs.7b01820.
- (10) Peter, L. M. Dynamic aspects of semiconductor photoelectrochemistry. *Chem. Rev.* **1990**, *90*, 753–769, DOI: 10.1021/cr00103a005.
- (11) Abrantes, L. Transient photocurrents at passive iron electrodes. *J. Electroanal. Chem.* **1983**, *150*, 593–601, DOI: 10.1016/0368-1874(83)80316-5.
- (12) Carroll, G. M.; Gamelin, D. R. Kinetic analysis of photoelectrochemical water oxidation by mesostructured Co-Pi/ α -Fe₂O₃ photoanodes. *J. Mater. Chem. A* **2016**, *4*, 2986–2994, DOI: 10.1039/C5TA06978E.
- (13) Monllor-Satoca, D.; Bärtsch, M.; Fàbrega, C.; Genç, A.; Reinhard, S.; Andreu, T.; Arbiol, J.; Niederberger, M.; Morante, J. R. What do you do, titanium?: Insight into the role of titanium oxide as a water oxidation promoter in hematite-based photoanodes. *Energy Environ. Sci.* **2015**, *8*, 3242–3254, DOI: 10.1039/C5EE01679G.
- (14) Hajibabaei, H.; Schon, A. R.; Hamann, T. W. Interface Control of Photoelectrochemical Water Oxidation Performance with Ni_{1-x}Fe_xO_y Modified Hematite Photoanodes. *Chem. Mater.* **2017**, *29*, 6674–6683, DOI: 10.1021/acs.chemmater.7b01149.